



Combustion stability and hetero-/homogeneous chemistry interactions for fuel-lean hydrogen/air mixtures in platinum-coated microchannels

Ran Sui, John Mantzaras*

Paul Scherrer Institute, Laboratory of Thermal Processes and Combustion, CH-5232 Villigen PSI, Switzerland



ARTICLE INFO

Article history:

Received 9 May 2016

Revised 16 August 2016

Accepted 17 August 2016

Available online 16 September 2016

Keywords:

Hetero-/homogeneous combustion of hydrogen over platinum

Combustion stability limits of hydrogen

Micoreactors

Detailed catalytic and gas-phase chemistry

Extinction

pressure dependence of stability limits

ABSTRACT

The hetero-/homogeneous combustion and stability limits of fuel-lean hydrogen/air mixtures (equivalence ratio $\varphi=0.40$) were investigated numerically in a platinum-coated planar microchannel with a length of 10 mm and a height of 1 mm. A two-dimensional numerical model was used for both the gas and the solid, which included elementary heterogeneous and homogeneous reaction mechanisms, detailed transport, heat conduction in the solid, surface radiation heat transfer, and external losses via a heat transfer coefficient h . Pressures of 1 and 5 bar and solid thermal conductivities $k_s = 1$ and $16 \text{ W m}^{-1} \text{ K}^{-1}$ were analyzed, while stability maps were constructed in terms of the critical extinction heat transfer coefficient h_{cr} versus inlet velocity U_{IN} (or mass throughput). For a given solid thermal conductivity, there existed a crossover mass throughput above (below) which the stability envelope was broader at 5 bar (1 bar). Simulations with a surface perfectly stirred reactor (SPSR) model qualitatively reproduced the crossover points, which originated from a shift in the pressure dependence of the catalytic reactivity of hydrogen. For the low solid thermal conductivity $k_s = 1 \text{ W m}^{-1} \text{ K}^{-1}$, a non-monotonic dependence of the stability limits on the mass throughput was shown, with local minima created below the crossover point. The stability limits of hydrogen were solely determined by catalytic chemistry, as it sustained combustion at temperatures down to 320–380 K, at which gas-phase chemistry was frozen. Away from the critical extinction points, both catalytic and gas-phase reaction pathways were controlling. The diffusional imbalance of hydrogen, which led to catalytically-induced superadiabatic surface temperatures, and the suppression of the surface superadiabicity by gaseous chemistry resulted in rich combustion phenomena, such as increasing peak wall temperatures with increasing heat transfer coefficients h . Critical extinction heat transfer coefficients for hydrogen were three to four orders of magnitude higher than those reported for methane and propane fuels in a similar channel geometry.

© 2016 The Combustion Institute. Published by Elsevier Inc. All rights reserved.

1. Introduction

Hydrogen-rich fuels have attracted increased attention in combustion methodologies aiming at the reduction of CO₂ greenhouse emissions [1]. In particular, hydrogen combustion is of interest for post-combustion CO₂ capture approaches, wherein flue gas recycle (FGR) is typically applied to increase the CO₂ content in the exhaust gas and thus facilitate its subsequent capture [2]. With increasing amounts of FGR, however, combustion stability deteriorates. An option to restore combustion stability is the addition of hydrogen (produced e.g. via catalytic partial oxidation of part of the fuel [3]) into the diluted reactive mixture [4]. Another approach for reduced greenhouse emission is the pre-combustion CO₂ capture, which involves decarbonization of the fossil fuel

(mainly coal, but also natural gas [5]) and subsequent combustion of a syngas mixture with high hydrogen content (> 80% vol.) [6,7]. Fundamental combustion characteristics of such syngas fuels are currently under intense investigation [8–10]. In addition to large-scale power generation, hydrogen and hydrogen-rich fuels are also of interest for micoreactors in portable power generation systems [11–14]. Such fuels can be produced from hydrocarbons using onboard microreformers [15–17].

For the aforementioned pre- and post-combustion CO₂ capture methodologies, hybrid concepts combining catalytic (heterogeneous) and gas-phase (homogeneous) combustion are under investigation. One such hybrid concept is the catalytically stabilized thermal combustion (CST) [18,19], in which part of the fuel is converted heterogeneously in a catalytic reactor and the rest is combusted in a downstream gas-phase burner. Both catalytic and gas-phase combustion modules in CST operate at fuel-lean stoichiometries. For pre-combustion CO₂ capture methods, the large amounts of hydrogen in the fuel mixture increase the risk of flame

* Corresponding author. Fax: +41 56 3102199.

E-mail address: ioannis.mantzaras@psi.ch (J. Mantzaras).

Nomenclature

b	channel half-height, Fig. 1
$c_{p,k}$	specific heat at constant pressure of k -th gaseous species, Eq. (7)
D_{km}	mixture-average diffusion coefficient of k -th gaseous species, Eq. (6)
D_k^T	thermal diffusion coefficient of k -th gaseous species, Eq. (6)
F_{k-j}	view factor between discretized channel surfaces k and j , Eq. (15)
h	total enthalpy, Eq. (4), heat transfer coefficient, Eqs. (12) and (18)
h_k^0	chemical enthalpy of the k -th gaseous species, Eq. (7)
K_g	total number of gaseous species, Eq. (4)
k_s	thermal conductivity of solid, Eqs. (8) and (9)
L, L_a, L_i	total, catalytically-coated, and catalytically-inert channel lengths, Fig. 1
Le	Lewis number (thermal over mass diffusivity)
M_s	total number of surface species, Eq. (11)
p	pressure, Eqs. (2) and (3)
q_k	radiation heat flux on k -th discretized surface element, Eq. (14)
q_{rad}	radiation heat flux, Eq. (9)
R	universal gas constant, Eq. (7)
\dot{s}_k	catalytic molar production rate of k -th species, Eq. (9)
S/V	surface to volume ratio, Eqs. (17) and (18)
T	temperature of gas
T_r	reactor temperature, Eq. (18)
T_{WALL}	wall temperature, Eqs. (8), (9) and (12)
T_0	reference temperature, Eq. (7)
T_∞	ambient temperature, Eq. (18)
u	streamwise velocity component Eqs. (1)–(3)
U_{IN}	inlet streamwise velocity
v	transverse ($-y$) velocity component, Eqs. (1)–(3)
\vec{V}_k	diffusion velocity vector of k -th gaseous species, Eq. (6)
W_k, \bar{W}	molecular weight of k -th gaseous species, average molecular weight
Y_k	mass fraction of k -th gaseous species
x, y	streamwise and transverse coordinates, Fig. 1

Greek Symbols

Γ	surface site density, Eq. (11)
δ_s	thickness of solid wall, Fig. 1
ε	surface emissivity, Eqs. (13) and (14)
θ_m	coverage of m -th surface species, Eq. (11)
λ_g	thermal conductivity of gas, Eq. (4)
μ	dynamic viscosity, Eqs. (2) and (3)
ρ	density of gas
σ	Stefan-Boltzmann constant, Eqs. (13) and (14)
σ_m	surface species site occupancy, Eq. (11)
τ	residence time, Eqs. (17) and (18)
φ	hydrogen-to-oxygen equivalence ratio
$\dot{\omega}_k$	homogeneous molar production rate of k -th species, Eq. (5)

Subscripts

cr	critical
IN, OUT	inlet, outlet
k, m	indices for gas-phase and surface species
WALL	wall

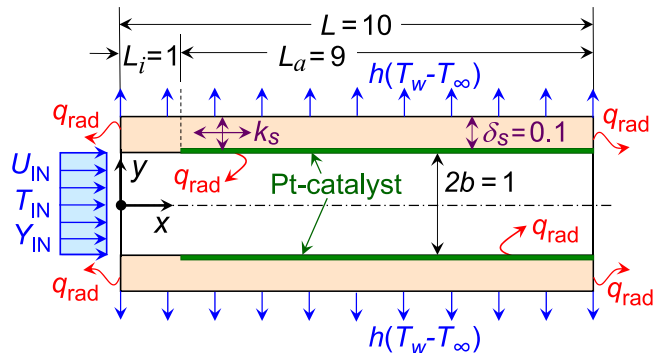


Fig. 1. Catalytic channel geometry. All dimensions are in mm.

flashback. To this direction, the CST hybrid concept negates flashback due to the presence of the catalytic module, which in turn inhibits upstream flame propagation [20]. Conversely, for the post-combustion CO₂ capture methods, the catalytic reactor increases the combustion stability of the less-reactive FGR-diluted fuels by lowering their effective ignition activation energy [19]. While hybrid hetero-/homogeneous combustion is a possibility for large-scale power generation, it is the preferred approach for microreactors. This is a result of the large surface-to-volume ratios of microreactors, the suppression of the various intrinsic flame instabilities in wall-bounded flows [21–25] by the presence of a catalyst [26,27], and the wider combustion stability envelopes of hetero-/homogeneous reactive systems compared to only homogeneous ones [28,29].

Recent studies have improved the understanding of gas-phase hydrogen kinetics, especially at elevated pressures relevant to power generation [8,30–32]. In addition, detailed mean-field catalytic reaction mechanisms for the oxidation of hydrogen on platinum (the catalyst of interest in the present study) have been developed [33–37]. Investigations of combined heterogeneous and homogeneous hydrogen combustion have also advanced. Appel et al. [38] employed in situ 1-D Raman measurements of major gas-phase species concentrations and 2-D laser induced fluorescence (LIF) of the OH radical in a Pt-coated channel and, in conjunction with numerical predictions, provided validated hetero-/homogeneous chemical reaction mechanisms for fuel-lean H₂/air mixtures at atmospheric pressure. Mantzaras et al. [39] and Ghermay et al. [40,41] extended the previous studies to pressures up to 15 bar, delineating the operating regimes where the competition between the two reaction pathways suppressed homogeneous combustion. Accompanying hetero-/homogeneous combustion experiments for fuel-rich H₂/air mixtures over Pt surfaces were reported in Schultze et al. [42]. In terms of simulations, fundamental hetero-/homogeneous kinetic studies were firstly reported by Bui et al. [43], who investigated the coupling of catalytic and gas-phase reactions for fuel-lean and fuel-rich H₂/air combustion in a stagnation point flow over a Pt surface at atmospheric pressure. Lately, Brambilla et al. [44] used 2-D direct numerical simulation (DNS) with conjugate heat transfer in the solid wall to study the transient combustion of fuel-lean H₂/air mixtures in a Pt-coated channel and to identify the main reactions controlling catalytic and gas-phase ignition.

Key issue in the design and thermal management of microreactors is the demarcation of stable combustion operating regimes. For gaseous combustion of methane/air and propane/air mixtures, stability was investigated numerically by Norton et al. [28,45] in channels with sub-millimeter gap sizes and chemically inert walls. They used 2-D simulations with a one-step gaseous reaction and assessed the impact of heat transfer mechanisms on the reactor energy management. For catalytic combustion of methane over Pt

(in the absence of gaseous reactions), extinction was investigated by Maruta et al. [46] using 2-D simulations and a detailed heterogeneous reaction mechanism in a 1-mm height channel with thermally-thin walls (no axial heat conduction in the solid). Furthermore, extinction limits were mapped out experimentally for either catalytic or non-catalytic combustion of propane/air mixtures in a heat recirculating Swiss-roll burner [47]. In all previous studies the pressure was atmospheric. For combined heterogeneous and homogeneous reactions, fewer combustion stability studies have been reported. Karagiannidis et al. [29] investigated numerically the combustion stability of fuel-lean methane/air mixtures in a Pt-coated microchannel with a height of 1 mm and prescribed external heat losses. They used a 2-D model for the gas and solid phases with detailed hetero-/homogeneous chemical reaction schemes and showed that the presence of gaseous chemistry appreciably extended the blowout limits due to the incomplete gas-phase combustion of CH_4 to CO and the ensuing catalytic oxidation of CO to CO_2 on the Pt surface. Subsequent propane/air hetero-/homogeneous combustion stability studies [48] have shown that, despite the lower catalytic and gas-phase reactivities of methane compared to those of propane, methane had appreciably broader blowout limits due to its higher molecular diffusivity that facilitated enhanced fuel consumption when the catalytic reactions were transport-limited.

Hydrogen has a high catalytic reactivity on platinum [49,50] and its diffusional imbalance (Lewis number $Le_{\text{H}_2} \sim 0.3$ at fuel-lean stoichiometries) leads to superadiabatic surface temperatures [19,51] that in turn endanger the reactor/catalyst thermal stability and promote the onset of homogeneous ignition. Detailed stability studies for hetero-/homogeneous combustion of hydrogen or high-hydrogen-content fuels relevant to new combustion methodologies have not yet been reported. Hydrogen-fueled catalytic microreactors are of interest in combined combustion/solar approaches [14], where it is desirable to maintain wide-enough stability envelopes for the stand-alone combustion mode so as to mitigate extinction in the event of a complete loss of power input from the supporting solar mode. Relevant past experimental studies, which addressed various aspects of hydrogen combustion over platinum, included Norton et al. [11] who investigated the ignitability of lean and rich H_2/air mixtures in channels with heights of 1.0 mm and 0.25 mm, Boyarko et al. [52] who measured ignition temperatures of fuel-rich H_2/air mixtures in platinum tubes with inner diameters of 0.4 and 0.8 mm, and Ghermay et al. [40] who demonstrated an inverse CST concept for fuel-lean H_2/air combustion (with the gaseous combustion zone preceding the catalytic reactor, so as to mitigate superadiabatic catalyst temperatures).

The present work undertakes a numerical investigation of the hetero-/homogeneous combustion stability limits of fuel-lean (equivalence ratio $\varphi=0.40$) H_2/air mixtures in a Pt-coated planar channel with a height of 1 mm and a length of 10 mm. Simulations are carried out using a 2-D elliptic model for the gas and solid phases, at pressures 1 and 5 bar. Detailed hetero-/homogeneous chemical reaction schemes are used, along with heat conduction in the solid walls, surface radiation heat transfer, and prescribed external heat losses. Main objective is to investigate the interactions of hydrogen hetero-/homogeneous chemistry, transport, and heat transfer mechanisms and to delineate combustion stability maps in terms of key parameters.

This paper is organized as follows. The numerical methodology and the adopted parameter ranges are presented in Section 2, while main results follow in Section 3. Fundamentals of hydrogen catalytic extinction (and ignition) and their dependence on pressure are presented in Section 3.1 by using a simpler configuration—the surface perfectly stirred reactor. Discussion of the combustion stability maps in the channel as a function of pressure, inlet

velocity and solid thermal conductivity follows in Sections 3.2 and 3.3, while comparisons with hetero-/homogeneous stability maps of methane and propane are elaborated in Section 3.4. Finally, conclusions are summarized in Section 4.

2. Numerical model

The 2-D steady code of PSI [38,48,53] was used to simulate the laminar flow in a plane channel with length $L=10$ mm, full height $2b=1$ mm and wall thicknesses $\delta_s = 0.1$ mm (see Fig. 1). The internal channel surfaces ($y=\pm b$) were catalytically inert over the initial length $L_i = 1$ mm and coated with platinum over the remaining length $L_a = 9$ mm. A 10 mm length has also been used in earlier fundamental extinction studies in channels (operating either in sole gas-phase combustion mode [45], sole catalytic combustion mode [46], or combined hetero-/homogeneous combustion modes [29,48]), while the 1 mm height was typical to the geometrical confinements of catalytic channels in practical honeycomb reactors; moreover, the geometry in Fig. 1 allowed for direct comparisons with earlier methane and propane hetero-/homogeneous combustion stability studies [29,48]. The channel wall thickness $\delta_s = 0.1$ mm was also typical for ceramic or metallic honeycomb catalytic reactors.

Two-dimensional heat conduction in the solid wall was accounted for, with two investigated solid thermal conductivities $k_s = 1$ and $16 \text{ Wm}^{-1}\text{K}^{-1}$, corresponding to cordierite (ceramic) and FeCr-alloy (metallic) materials, respectively. External heat losses were applied to the outer channel surfaces $y=\pm(b+\delta_s)$, modeled as $q_{\text{loss}}(x) = h[T_{\text{WALL}}(x, y=b+\delta_s) - T_\infty]$, with h the heat transfer coefficient, $T_\infty = 300$ K, and T_{WALL} the local outer wall temperature.

Hydrogen/air was fed into the channel with a fuel-lean equivalence ratio $\varphi=0.40$, uniform inlet temperature $T_{\text{IN}} = 300$ K, uniform inlet velocity U_{IN} , and an incoming pressure of either 1 or 5 bar (the higher pressure was relevant to microturbine-based microreactors [54]). Radiation exchange between the discretized inner surface elements, as well as between the surface elements themselves and the inlet and outlet channel enclosures was accounted for by the net radiation method for diffuse-gray areas [29,55]. The inlet velocity U_{IN} and the heat transfer coefficient h were the two main parameters varied in the ensuing studies.

2.1. Governing equations

Due to symmetry, half of the channel domain ($0 \leq y \leq b + \delta_s$ in Fig. 1) was modeled. The governing equations for a steady, laminar flow with homogeneous and heterogeneous chemical reactions in Cartesian coordinates are:

Continuity equation:

$$\frac{\partial(\rho u)}{\partial x} + \frac{\partial(\rho v)}{\partial y} = 0. \quad (1)$$

Momentum equations:

$$\begin{aligned} \frac{\partial(\rho uu)}{\partial x} + \frac{\partial(\rho vu)}{\partial y} + \frac{\partial p}{\partial x} - \frac{\partial}{\partial x} \left[2\mu \frac{\partial u}{\partial x} - \frac{2}{3}\mu \left(\frac{\partial u}{\partial x} + \frac{\partial v}{\partial y} \right) \right] \\ - \frac{\partial}{\partial y} \left[\mu \left(\frac{\partial u}{\partial y} + \frac{\partial v}{\partial x} \right) \right] = 0, \end{aligned} \quad (2)$$

$$\begin{aligned} \frac{\partial(\rho uv)}{\partial x} + \frac{\partial(\rho vv)}{\partial y} + \frac{\partial p}{\partial y} - \frac{\partial}{\partial y} \left[\mu \left(\frac{\partial u}{\partial y} + \frac{\partial v}{\partial x} \right) \right] \\ - \frac{\partial}{\partial y} \left[2\mu \frac{\partial v}{\partial y} - \frac{2}{3}\mu \left(\frac{\partial u}{\partial x} + \frac{\partial v}{\partial y} \right) \right] = 0. \end{aligned} \quad (3)$$

Energy equation:

$$\begin{aligned} \frac{\partial(\rho u h)}{\partial x} + \frac{\partial(\rho v h)}{\partial y} + \frac{\partial}{\partial x} \left(\rho \sum_{k=1}^{K_g} Y_k h_k V_{k,x} - \lambda_g \frac{\partial T}{\partial x} \right) \\ + \frac{\partial}{\partial y} \left(\rho \sum_{k=1}^{K_g} Y_k h_k V_{k,y} - \lambda_g \frac{\partial T}{\partial y} \right) = 0. \end{aligned} \quad (4)$$

Gas-phase species equations:

$$\begin{aligned} \frac{\partial(\rho u Y_k)}{\partial x} + \frac{\partial(\rho v Y_k)}{\partial y} + \frac{\partial}{\partial x} (\rho Y_k V_{k,x}) + \frac{\partial}{\partial y} (\rho Y_k V_{k,y}) - \dot{\omega}_k W_k = 0, \\ k = 1, \dots, K_g. \end{aligned} \quad (5)$$

The species diffusion velocities $V_{k,x}$ and $V_{k,y}$ in Eqs. (4) and (5) were computed using a mixture-average transport model including thermal diffusion [56]:

$$\vec{V}_k = -D_{km} \vec{\nabla} \left(\ln \frac{Y_k \bar{W}}{W_k} \right) - \frac{D_k^T W_k}{\rho Y_k \bar{W}} \vec{\nabla} (\ln T), \quad k = 1, \dots, K_g. \quad (6)$$

Finally, the ideal gas and caloric equations of state were:

$$p = \frac{\rho R T}{\bar{W}} \text{ and } h_k = h_k^0(T_0) + \int_{T_0}^T c_{p,k} dT, \quad k = 1, \dots, K_g. \quad (7)$$

For the 2-D solid domain, the heat conduction equation was solved:

$$\frac{\partial}{\partial x} \left(k_s \frac{\partial T_{WALL}}{\partial x} \right) + \frac{\partial}{\partial y} \left(k_s \frac{\partial T_{WALL}}{\partial y} \right) = 0. \quad (8)$$

The gas-phase Eqs. (1)–(5), supplemented with the auxiliary Eqs. (6) and (7), and the solid energy Eq. (8) were solved subject to appropriate boundary conditions. At the gas-solid interface ($y=b$), the energy and gas-phase species boundary conditions were:

$$q_{rad} - \left(\lambda_g \frac{\partial T}{\partial y} \right)_{y=b^-} + \left(k_s \frac{\partial T_{WALL}}{\partial y} \right)_{y=b^+} + B \sum_{k=1}^{K_g} (\dot{s}_k h_k W_k)_{y=b} = 0, \quad (9)$$

$$(\rho Y_k V_{k,y})_{y=b} + B \dot{s}_k W_k = 0, \quad k = 1, \dots, K_g, \quad (10)$$

respectively, with \dot{s}_k the heterogeneous molar production rate of the k th gaseous species and q_{rad} the incident radiation flux. In Eqs. (9) and (10), $\dot{s}_k = 0$ over the catalytically-inert length $0 \leq x \leq L_i$. The factor B denoted the ratio of the catalytically-active to the geometrical surface area and was herein considered unity, simulating a polycrystalline platinum surface. For supported technical catalysts, B can be determined experimentally [57]. The surface species coverage equations were:

$$\begin{aligned} \theta_m = 0 \text{ for } 0 \leq x \leq L_i \text{ and } \partial \theta_m / \partial t - \sigma_m \dot{s}_m / \Gamma = 0 \text{ for} \\ L_i < x \leq L, \quad m = 1, \dots, K_s. \end{aligned} \quad (11)$$

The $\partial \theta_m / \partial t$ in the left side of Eq. (11) was not a true transient term and was only introduced to facilitate convergence of the Newton solver for the algebraic surface species coverage equations [58]. At the outer channel horizontal surface ($y = b + \delta_s$):

$$\begin{aligned} -k_s \frac{\partial T_{WALL}(x, y)}{\partial y} \Big|_{y=(b+\delta_s)^-} \\ = h [T_{WALL}(x, y = b + \delta_s) - T_\infty] \text{ for } 0 \leq x \leq L, \end{aligned} \quad (12)$$

with $T_\infty = 300$ K. Radiative boundary conditions were applied to the front and rear vertical solid wall faces ($x=0$ or L , and $b < y \leq b + \delta_s$) with an emissivity $\varepsilon = 0.60$:

$$\begin{aligned} k_s \frac{\partial T_{WALL}}{\partial x} \Big|_{x=0^+} &= \varepsilon \sigma [T_{WALL}^4(x=0, y) - T_{IN}^4] \text{ and} \\ -k_s \frac{\partial T_{WALL}}{\partial x} \Big|_{x=L^-} &= \varepsilon \sigma [T_{WALL}^4(x=L, y) - T_{OUT}^4]. \end{aligned} \quad (13)$$

In Eq. (13) the inlet and outlet radiation exchange temperatures were set equal to the inlet gas and the outlet gas mixing cup temperatures, respectively. For the inner catalytic channel surfaces, the radiative heat balance was:

$$\frac{1}{\varepsilon_k} q_k = \sum_{j=1}^{N+2} F_{k-j} \sigma (T_k^4 - T_j^4) + \sum_{j=1}^{N+2} \left(\frac{1 - \varepsilon_j}{\varepsilon_j} \right) F_{k-j} q_j, \quad (14)$$

with q_k representing the net radiation flux for the k th discretized inner surface element and the index j runs over the total N catalytic surface elements as well as the inlet ($j=N+1$) and outlet ($j=N+2$) enclosures. Catalytic surface emissivities were $\varepsilon_j = 0.60$, while the inlet and outlet were treated as black bodies ($\varepsilon_{N+1} = \varepsilon_{N+2} = 1.0$). The geometrical view factors F_{k-j} between the upper-wall and lower-wall channel surface elements k and j , respectively, for two parallel plates placed at a distance $2b$ apart were [55,59]:

$$\begin{aligned} F_{k-j} = \frac{1}{2(x_{k+1} - x_k)} &\left([(2b)^2 + (x_{k+1} - x_j)^2]^{1/2} \right. \\ &- [(2b)^2 + (x_{k+1} - x_{j+1})^2]^{1/2} + [(2b)^2 + (x_k - x_{j+1})^2]^{1/2} \\ &\left. - [(2b)^2 + (x_k - x_j)^2]^{1/2} \right), \quad j = 1, \dots, N. \end{aligned} \quad (15)$$

Finally, the view factors between the discretized k th surface element and the inlet ($N+1$) and outlet ($N+2$) enclosures were:

$$\begin{aligned} F_{k-(N+1)} = \frac{1}{2(x_{k+1} - x_k)} &\left([(2b)^2 + (x_k)^2]^{1/2} - [(2b)^2 + (x_{k+1})^2]^{1/2} \right. \\ &+ (x_{k+1} - x_k) \Big) \text{ and} \\ F_{k-(N+2)} = \frac{1}{2(x_{k+1} - x_k)} &\left([(2b)^2 + (x_{k+1} - L)^2]^{1/2} \right. \\ &- [(2b)^2 + (x_k - L)^2]^{1/2} + (x_{k+1} - x_k) \Big) \end{aligned} \quad (16)$$

with the k th surface element extending over $x_k \leq x < x_{k+1}$.

An orthogonal staggered grid with 140×48 points (in x and y , respectively) was used to discretize half the flow domain ($10 \times 0.5 \text{ mm}^2$), with finer spacing towards the channel wall and the inlet. The solid wall was discretized by 140×20 points in x and y , respectively. The employed gas-phase and solid-phase meshes were sufficient to produce a grid-independent solution, as shown by successive grid refinements. Uniform profiles of species, temperature and axial velocity were considered at the inlet, while zero-Neumann conditions were set at the outlet ($x=L$) and the plane of symmetry ($y=0$). No-slip was applied for both velocity components at the gas-wall interface ($y=b$). Details of the solution algorithm have been provided elsewhere [38,40,58].

While 3-D catalytic reactor models with conjugate heat transfer have been used in the literature (either with a one-step catalytic reaction [60] or with detailed catalytic chemistry [14,61]), two-dimensional geometries, such as the one in Fig. 1, are standard in computationally demanding criticality extinction studies [29,45,46] especially when detailed hetero-/homogeneous chemistry is included [29]. Moreover, 2-D models are adequate for a class of practical catalytic rectangular reactors with high cross-flow aspect ratios, as in Norton et al. [11] (aspect ratios 10–40).

2.2. Chemical kinetics

For hydrogen oxidation on platinum, the detailed heterogeneous scheme of Deutschmann et al. [36] (11 irreversible and 3

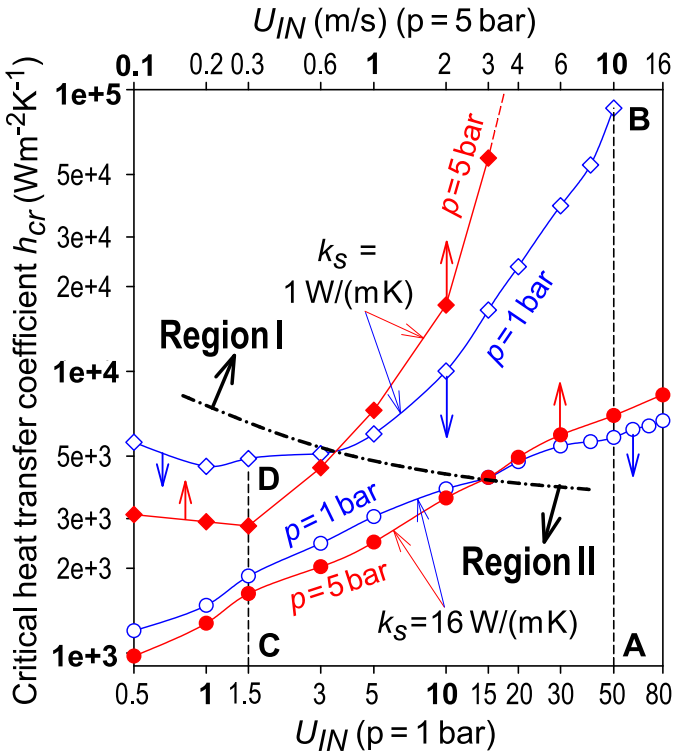


Fig. 2. Computed stability diagrams of an H₂/air mixture ($\varphi=0.40$) in the channel of Fig. 1 for two pressures (1 bar: open symbols, 5 bar: filled symbols) and two solid thermal conductivities ($k_s = 1 \text{ Wm}^{-1}\text{K}^{-1}$: diamonds, $k_s = 16 \text{ Wm}^{-1}\text{K}^{-1}$: circles).

reversible reactions, 5 surface and 6 gaseous species) was used, with a surface site density $\Gamma=2.7 \times 10^{-9} \text{ mol/cm}^2$. Surface thermodynamic data for the three reversible reactions were taken from [62]. For homogeneous chemistry, the H₂/O₂ elementary reaction mechanism from Li et al. [30] was employed (21 reversible reactions and 9 species) with its accompanying gas-phase thermodynamic data.

The above hetero-/homogeneous reaction mechanisms have been shown to reproduce measured homogeneous ignition characteristics and post-ignition flame shapes (assessed via planar laser induced fluorescence of OH) in a Pt-coated channel, for fuel-lean H₂/air stoichiometries and pressures up to 15 bar [39,41]. More recently, these mechanisms were further validated for fuel-rich H₂/air hetero-/homogeneous combustion over Pt at pressures up to 5 bar [42]. Surface and gas-phase reaction rates were evaluated using Surface Chemkin [63] and Chemkin [64], respectively, while transport properties were calculated from the Chemkin database [56].

3. Results and discussion

Simulations were carried out by varying the external heat transfer coefficient h and the inlet velocity U_{IN} . Additionally, two solid thermal conductivities $k_s=1$ and $16 \text{ Wm}^{-1}\text{K}^{-1}$ (corresponding to cordierite and FeCr-alloy reactor materials, respectively) and two pressures $p=1$ and 5 bar were examined. In all cases, the inlet H₂/air mixture had a fuel-to-air equivalence ratio $\varphi=0.40$ and $T_{IN}=300 \text{ K}$. Stability limits were constructed by one-parameter continuation: for a given U_{IN} the heat transfer coefficient h was progressively increased from zero (corresponding to the vigorous burning solution) until a critical extinction value h_{cr} was reached. Figure 2 presents four such stability curves (h_{cr} versus U_{IN} in logarithmic scales) for the two investigated pressures and two solid thermal conductivities. The determination of critical extinc-

tion points was computationally intensive. As extinction was approached, the number of iterations in the CFD code increased exponentially since combustion was barely sustained. Moreover, the Δh increments had to be fine enough ($\sim 10 \text{ Wm}^{-2}\text{K}^{-1}$ or less) close to extinction. Finally, to ensure that the extinction limits had been approached, Δh was first coarsened (so as to identify the extinguished domain) and then refined in an iterative procedure to accurately determine the critical points. Each critical point in Fig. 2 required on the average three weeks in a single 2.3 GHz CPU.

To facilitate comparisons of stability limits at a given mass throughput ($\rho_{IN}U_{IN}b$), two different velocity axes, scaled by a factor of five, were used for $p=1$ and 5 bar . At a given abscissa location in Fig. 2, the mass throughput was the same for the two pressures. Velocities higher than 80 m/s at 1 bar (16 m/s at 5 bar) were not investigated as the incoming Reynolds numbers based on the channel height exceeded 4000. Moreover, velocities $U_{IN} > 100 \text{ m/s}$ (Mach number $Ma > 0.3$) would invalidate the low-Mach number formulation of Eqs. (1)–(5). The lower velocity range ($< 5 \text{ m/s}$ at $p=1 \text{ bar}$) in Fig. 2 referred to microreactor applications for portable power generation, whereas higher velocities ($> 20 \text{ m/s}$ at $p=1 \text{ bar}$) pertained to large-scale power generation. Moreover, the equivalence ratio $\varphi=0.40$ was consistent with the fuel-lean CST power generation methodologies mentioned in the Introduction and facilitated catalyst and reactor thermal management.

Areas below the stability lines in Fig. 2 denote stable combustion while areas above these lines are extinguished states. To clarify the behavior in Fig. 2, the chemical and flow processes controlling catalytic extinction, and ignition as well, of H₂/air mixtures over platinum as a function of pressure were firstly investigated using a simplified model, the surface perfectly stirred reactor. The stability plots in Fig. 2 are obtained using a steady model (similar to [29,45,46,48]) and have practical analogues in experiments where the continuation parameter is varied slowly in time such that a sequence of “quasisteady” states can be obtained: for example, typical extinction studies in catalytic reactors are performed by reducing the inlet temperature slowly by a few degrees K/min [65].

3.1. Hydrogen ignition and extinction kinetics

In a recent work on the ignition of fuel-lean H₂/air mixtures [66], we have demonstrated that rising pressures inhibited the onset of catalytic ignition over Pt due to the increased partial pressures of hydrogen that in turn accentuated the surface blockage by H(s). To analyze catalytic extinction and to also summarize the ignition behavior of hydrogen, simulations in an adiabatic surface perfectly stirred reactor (SPSR) [67] are shown in Fig. 3(a), whereby the stable weakly reacting and vigorous burning branches were constructed at 1 and 5 bar via one-parameter continuation, with selected parameter the SPSR residence time. The simulations included only catalytic chemistry, the SPSR inlet temperature was $T_{IN}=300 \text{ K}$, and the surface-to-volume ratio (S/V) was 20 cm^{-1} (same as the S/V of the channel in Fig. 1, when considering the entire internal channel surface and not only the catalytically coated one).

The corresponding H(s) coverages are plotted for the two pressures in Fig. 3(b). To facilitate comparison of the 1 and 5 bar results, two axes with a scaling factor of five are provided for the residence times (τ) in Fig. 3. For a given abscissa location in Fig. 3 the ratio ρ/τ was the same at both pressures (or equivalently the mass flow rate $\dot{m}=\rho V/\tau$ was the same at both pressures for a given reactor volume V). This allowed to directly assess the dependence of the catalytic reactivity on pressure since, for a given ρ/τ and S/V , the species consumption and the reactor temperature depended solely on the catalytic reaction rate s_k as

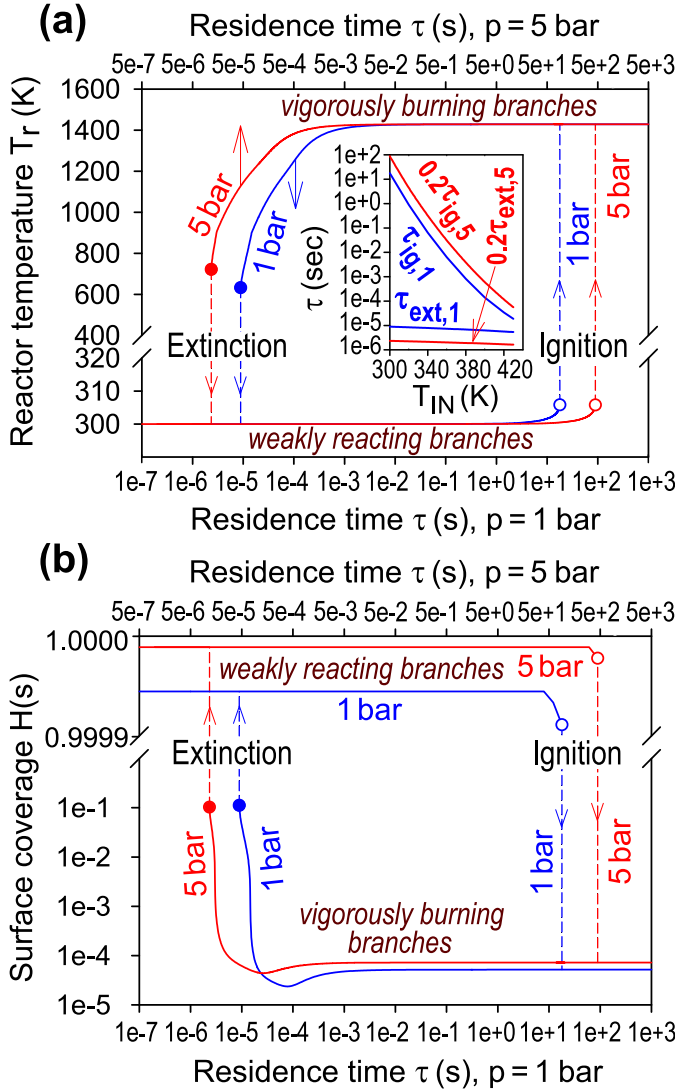


Fig. 3. Simulations in an adiabatic perfectly stirred reactor (SPSR) for an H_2/air mixture with $\varphi=0.40$, $T_{IN}=300 \text{ K}$, $S/V=20 \text{ cm}^{-1}$ and pressures of 1 and 5 bar: (a) reactor temperature T_r and (b) surface coverage of $\text{H}(s)$, versus residence time τ . Symbols define the points of ignition (open circles) and extinction (filled circles). The inset figure in (a) provides the ignition (τ_{ig}) and extinction (τ_{ext}) residence times at 1 bar (subscript 1) and 5 bar (subscript 5) versus T_{IN} .

evidenced by the SPSR conservation equations [67]:

$$(\rho/\tau)(Y_{k,OUT} - Y_{k,IN}) = (S/V)\dot{s}_k W_k, \quad k = 1, 2, \dots, K_g, \quad (17)$$

$$\begin{aligned} & (\rho/\tau) \sum_{k=1}^{K_g} Y_{k,IN} (h_{k,IN} - h_{k,OUT}) \\ &= (S/V) \sum_{k=1}^{K_g} (\dot{s}_k h_k W_k)_{y=b} - (S/V) h(T_r - T_\infty). \end{aligned} \quad (18)$$

In Eq. (18) h was the external heat transfer coefficient ($h=0$ for the adiabatic simulations in Fig. 3), T_r the reactor temperature and $T_\infty = T_{IN} = 300 \text{ K}$. Ignition was promoted at lower pressures, as manifested by the shorter ignition residence time at $p=1$ bar compared to 5 bar (Fig. 3(a)). Additionally, on the weakly reacting branches and prior to ignition the surface was predominantly covered by $\text{H}(s)$ (Fig. 3(b)), which blocked the adsorption of oxygen and inhibited ignition. Ignition was more favorable at 1 bar due

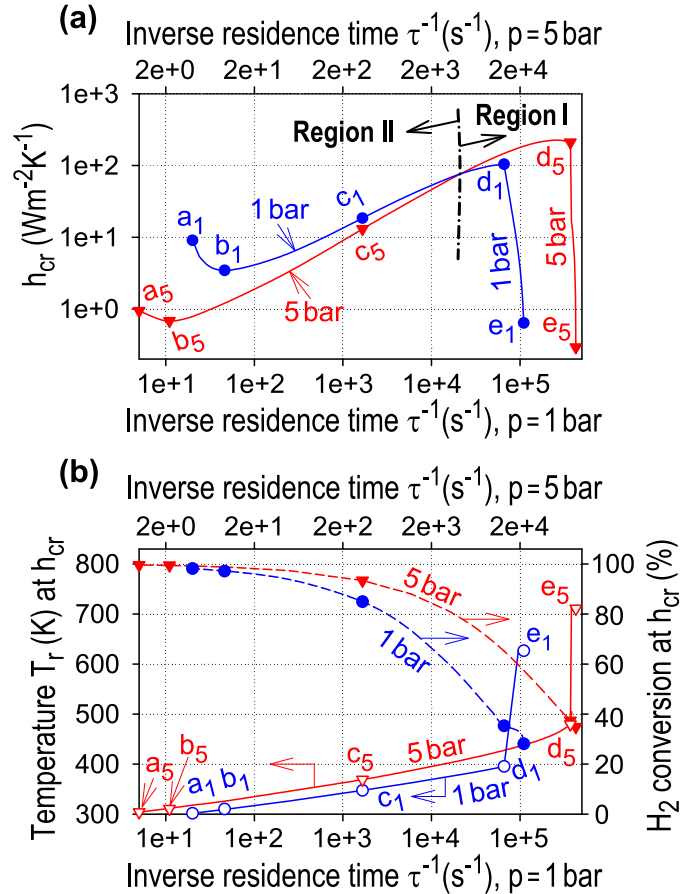


Fig. 4. Simulations in a non-adiabatic surface perfectly stirred reactor (SPSR) for an H_2/air mixture with $\varphi=0.40$, $T_{IN}=300 \text{ K}$, $S/V=20 \text{ cm}^{-1}$ and pressures of 1 and 5 bar. (a) Critical extinction points in the $h - \tau^{-1}$ parameter space (heat transfer coefficient versus inverse residence time), and (b) reactor temperature T_r and percent hydrogen conversion at the critical extinction points.

to its slightly lower $\text{H}(s)$ coverage on the weakly reacting branch compared to the corresponding $\text{H}(s)$ coverage at 5 bar.

While on the one hand lower pressures facilitated catalytic ignition, on the other hand they promoted extinction as seen by the narrower hysteresis (longer scaled extinction residence times) at 1 bar in Fig. 3(a). This opposite behavior was due to a change in chemistry after ignition, which led to a positive pressure dependence of the catalytic reactivity on the vigorously burning branch, according to $\dot{s}_{\text{H}_2} \sim p^{0.97}$ (at least for temperatures above 1000 K, as discussed in [66]). The inset in Fig. 3(a) provides ignition and extinction residence times at 1 and 5 bar as a function of the inlet temperature T_{IN} (the 5 bar data have been again rescaled by a factor of 1/5 such that the ratios ρ/τ were constant when changing pressure at a given T_{IN}). The scaled ignition residence times τ_{ig} dropped rapidly with increasing T_{IN} and, moreover, ignition was always more favorable at 1 bar. Conversely, the extinction residence times τ_{ext} dropped only modestly with rising T_{IN} and extinction was always more favorable at $p=1$ bar.

The impact of external heat losses on SPSR extinction was studied by additional one-parameter continuations, whereby for every point on the vigorously burning branches in Fig. 3(a), the external heat transfer coefficient h was progressively increased from zero until a critical extinction value h_{cr} was reached. Plots of critical h_{cr} versus inverse residence times τ^{-1} are shown in Fig. 4(a) for the two pressures: again two τ^{-1} scales were used for $p=1$ and 5 bar. The use of inverse residence times τ^{-1} in Fig. 4 assisted comparisons with the channel results in Fig. 2, since $\tau^{-1} \sim U_{IN}$. The

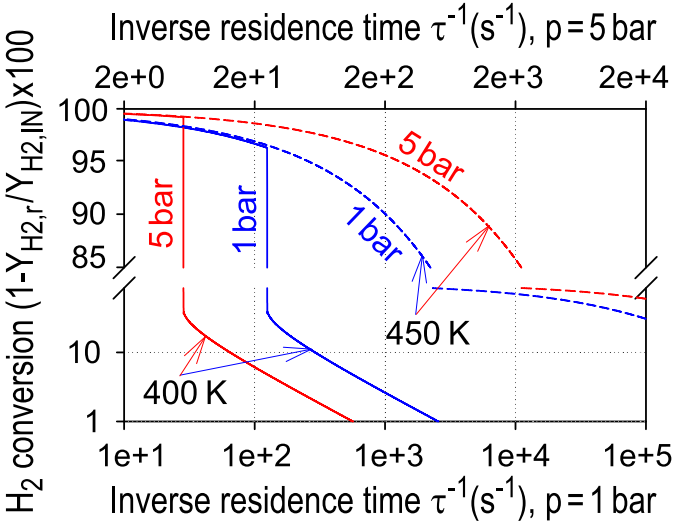


Fig. 5. Hydrogen conversions in an isothermal surface perfectly stirred reactor (SPSR) with $S/V=20 \text{ cm}^{-1}$ for an H_2/air mixture with $\varphi=0.40$, at $p=1$ and 5 bar and two reactor temperatures of 400 K (solid lines) and 450 K (dashed lines).

qualitative similarity of the plots in Figs. 4(a) and Fig. 2 was evident, with the following common features in the two figures: a) the existence of crossover scaled U_{IN} or τ^{-1} values, above (below) which the h_{cr} were higher (lower) at 5 bar, demarcating Regions I and II, and b) the presence of initial sections along the stability lines where h_{cr} decreased with rising U_{IN} (at least for the lower $k_s=1 \text{ Wm}^{-1}\text{K}^{-1}$ in Fig. 2) or with rising τ^{-1} (segments a_1b_1 and a_5b_5 in Fig. 4(a)), thus leading to the creation of local stability minima. The steep dropping segments d_1e_1 and d_5e_5 in Fig. 4(a) at very high τ^{-1} demarcated blowout limits and had no analogues in Fig. 2 due to the imposed upper limits in the investigated U_{IN} . Analysis of the processes in various segments of the stability diagrams in Fig. 4(a) is discussed next.

The rise of h_{cr} with decreasing τ^{-1} along segments b_1a_1 and b_5a_5 in Fig. 4(a) was due to the very low reactor temperatures attained at the corresponding long residence times. Characteristically, along b_1a_1 and b_5a_5 the critical reactor temperatures dropped monotonically and spanned the ranges 310.2–301.6 K and 310.6–303.9 K, respectively (see Fig. 4(b)). As these temperatures were close to $T_\infty=300$ K, the heat loss term $h(T_r - T_\infty)$ in Eq. (18) was minimal such that the reactor could tolerate increasingly higher h_{cr} with dropping τ^{-1} . Finally, despite the low reactor temperatures along b_1a_1 and b_5a_5 , the associated long residence times led to high H_2 conversions (97.1–98.2% and 99.4–99.6%, respectively, see Fig. 4(b)).

The crossover point in Fig. 4(a) delineating Regions I and II had chemical origins. To decouple thermal from chemical effects, additional SPSR simulations were performed at isothermal conditions with temperatures in the range 350–490 K, which were representative of the critical reactor temperatures along c_1d_1 and c_5d_5 (see Fig. 4(b)). Hydrogen catalytic conversions are plotted in Fig. 5 for $p=1$ and 5 bar as a function of τ^{-1} for 400 and 450 K. While at the lower temperature 400 K the conversion was higher at 1 bar over the bulk of the investigated τ^{-1} , at 450 K the conversion was higher at 5 bar. This indicated a shift in the pressure dependence of the hydrogen catalytic kinetics according to Eq. (17), which was in turn responsible for the observed crossover of the $p=1$ and 5 bar curves in Fig. 4(a).

The surface coverage at the critical extinction conditions of Fig. 4(a) is plotted in Fig. 6. Below the crossover point, in Region II of Fig. 4(a), $\text{H}_2\text{O}(s)$ was the dominant surface species, while $\text{H}(s)$ increased sharply along the final blowout lines d_1e_1 and d_5e_5 .

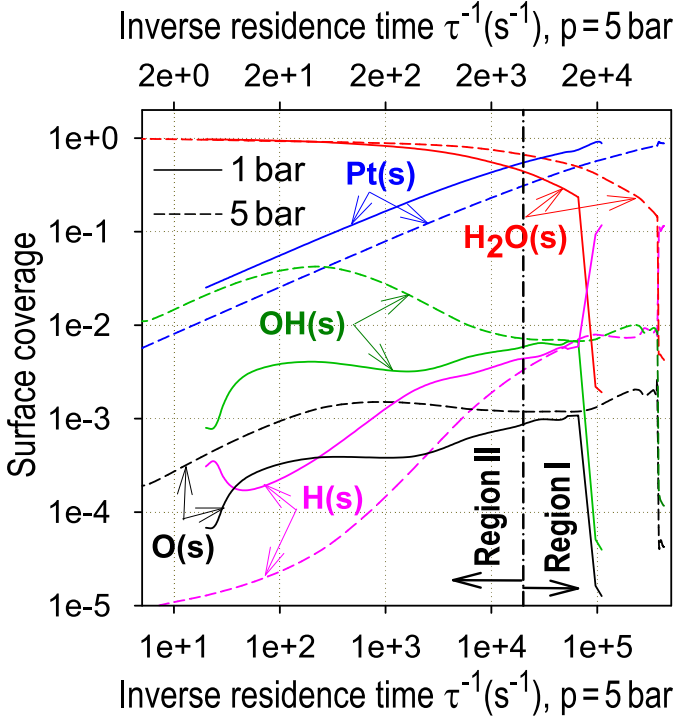


Fig. 6. Surface coverage along the extinction lines in Fig. 4(a) (solid lines: 1 bar, dashed lines: 5 bar).

Surface blockage by $\text{H}_2\text{O}(s)$ (i.e. product poisoning) near extinction was also reported by Vlachos and Bui [50] for 1% vol. H_2 in air in stagnation point-flow simulations over Pt, however, using a different catalytic reaction mechanism.

The key reactions affecting extinction were finally identified by means of sensitivity analysis (SA) along the critical lines in Fig. 4(a). The main reactions controlling the reactor temperature are shown in Fig. 7, where the normalized sensitivity coefficients are plotted at the selected points a_1 , c_1 , d_1 and e_1 in Fig. 4(a), referring to $p=1$ bar. The corresponding 5 bar SA yielded qualitatively similar results and is not shown.

For the critical points a_1 , c_1 and d_1 in Fig. 4(a), the key surface reactions were essentially the same (note the logarithmic scale in Fig. 7). The two controlling reactions were the hydrogen adsorption (R1) with a positive sensitivity and the oxygen adsorption (duplicate reactions R4 and R5) with negative sensitivity coefficient. This was because at sufficiently long residence times (low τ^{-1}) most of the surface was covered by $\text{H}_2\text{O}(s)$ (Fig. 6) such that an increase in hydrogen adsorption rendered combustion more resilient to extinction. At the blowout limits (point e_1), however, hydrogen coverage became significant and an increase of R1 promoted extinction (negative sensitivity of R1). Therein, increased hydrogen desorption (R2) or oxygen adsorption (R4, R5) stabilized combustion. Water adsorption (R8) always had a negative SA coefficient (and conversely, water desorption R9 had a positive coefficient) but with a progressively increasing impact along the entire limit line a_1e_1 . In summary, while lack of hydrogen controlled extinction along a_1d_1 , along the blowout line d_1e_1 the dominant extinction mechanism was lack of surface oxygen.

3.2. Combustion stability in the microchannel at high velocities

The crossover velocity U_{IN} in Fig. 2, above which the combustion stability limits at 5 bar were broader than those at 1 bar, was $\sim 3 \text{ m/s}$ at 1 bar ($\sim 0.6 \text{ m/s}$ at 5 bar) for $k_s=1 \text{ Wm}^{-1}\text{K}^{-1}$, increasing considerably to $\sim 15 \text{ m/s}$ at 1 bar ($\sim 3 \text{ m/s}$ at 5 bar) for

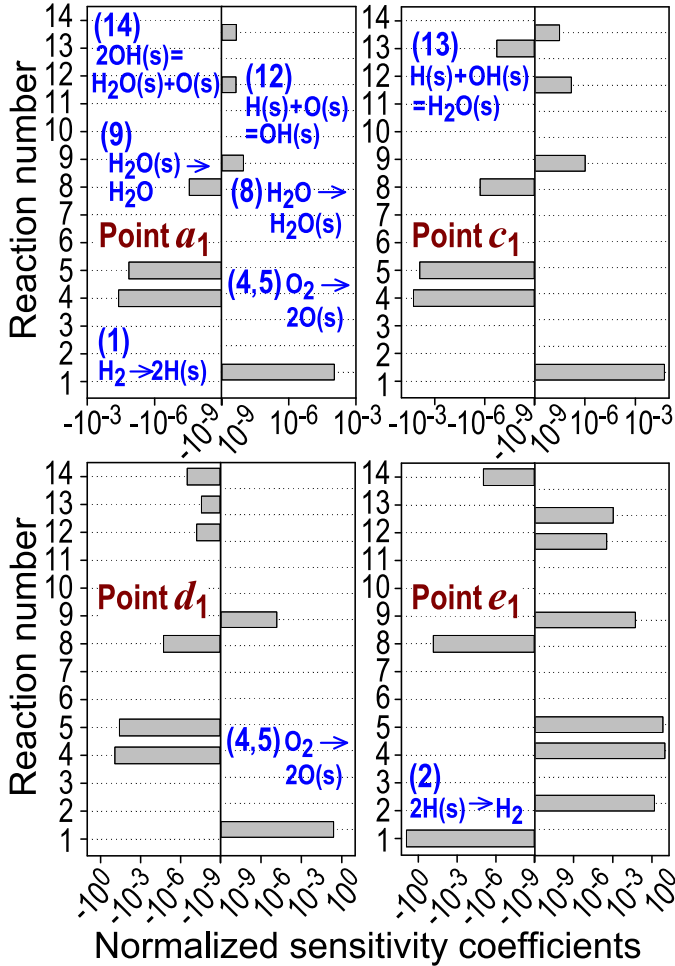


Fig. 7. Normalized sensitivity coefficients of temperature in a surface perfectly stirred reactor, at various critical extinction points for $p=1$ bar. The plots refer to points a_1 , c_1 , d_1 and e_1 in Fig. 4(a). Only surface reactions with sensitivity coefficient magnitudes larger than 10^{-9} are shown.

$k_s = 16 \text{ Wm}^{-1}\text{K}^{-1}$. In this section, the stability for U_{IN} above the crossover points, marked as Region I in Fig. 2, is analyzed.

Streamwise wall temperature profiles are illustrated in Fig. 8 for the two investigated pressures and two solid thermal conductivities and for various heat loss coefficients h at the high velocity $U_{IN}=50 \text{ m/s}$ ($p=1$ bar) or 10 m/s ($p=5$ bar) pertaining to Region I in Fig. 2. All plots in Fig. 8 fall along the line marked AB in Fig. 2. The wall temperatures T_{WALL} in Fig. 8 and in all subsequent plots, refer to the gas-wall interface ($y=b$ in Fig. 1); typically, for a given axial position x , differences in temperatures within the solid ($b \leq y \leq b+\delta_s$) were less than 40 K as will be shown in the coming Section 3.3. Heat transfer coefficients in Fig. 8 ranged from $h=0$ (nearly adiabatic, as there were still radiation losses from the catalytic channel surfaces and from the vertical wall faces to the inlet/outlet according to Eqs. (13) and (14)) to values close to the critical heat transfer coefficient for extinction h_{cr} . An exception was Fig. 4(b) at $p=5$ bar and $k_s=1 \text{ Wm}^{-1}\text{K}^{-1}$, for which h_{cr} was not reached even for the highest investigated $h=10^5 \text{ Wm}^{-2}\text{K}^{-1}$ (see also Fig. 2).

3.2.1. Hetero-/homogeneous combustion at low heat transfer coefficients h

At sufficiently low values of h , combined hetero-/homogeneous combustion occurred. Homogeneous combustion, in turn, greatly impacted the attained peak wall temperatures. For modest

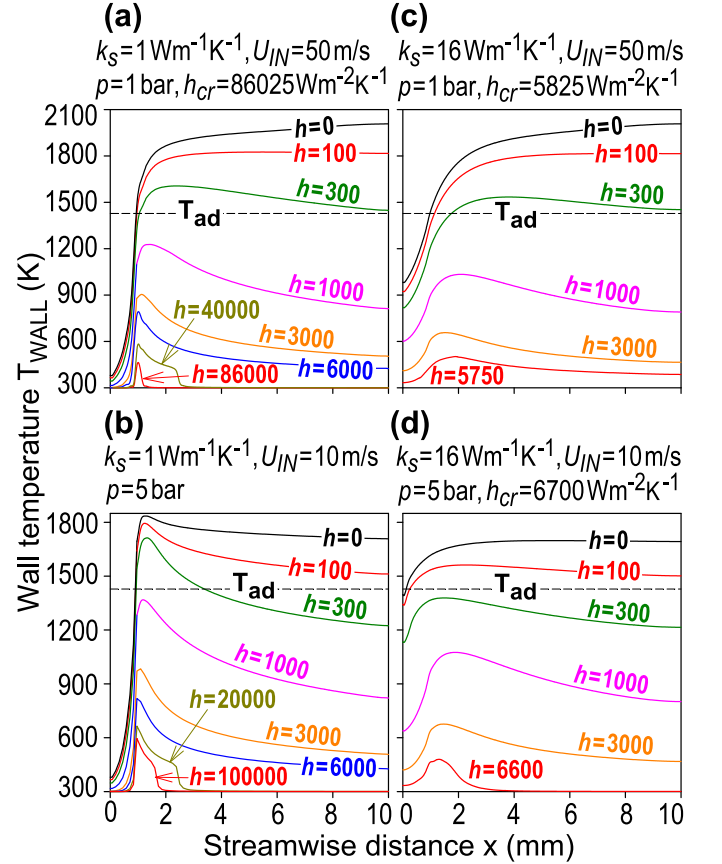


Fig. 8. Streamwise profiles of channel wall temperatures for various heat transfer coefficients h , ranging from 0 to values close to the critical h for extinction (h_{cr}). (a) $p=1$ bar, $U_{IN}=50 \text{ m/s}$, $k_s = 1 \text{ Wm}^{-1}\text{K}^{-1}$, (b) $p=5$ bar, $U_{IN} = 10 \text{ m/s}$, $k_s = 1 \text{ Wm}^{-1}\text{K}^{-1}$, (c) $p=1$ bar, $U_{IN}=50 \text{ m/s}$, $k_s = 16 \text{ Wm}^{-1}\text{K}^{-1}$ and (d) $p=5$ bar, $U_{IN} = 10 \text{ m/s}$, $k_s = 16 \text{ Wm}^{-1}\text{K}^{-1}$. Horizontal dashed lines marked T_{ad} provide the adiabatic equilibrium temperature (= 1428.5 K) of the incoming H_2/air mixture.

h ($\leq 300 \text{ Wm}^{-2}\text{K}^{-1}$) and for both investigated k_s , the simulations at $p=1$ bar in Fig. 8(a, c) yielded wall temperatures at least 200 K higher than the corresponding ones at $p=5$ bar in Fig. 8(b, d). Moreover, the diffusional imbalance of the hydrogen limiting reactant ($Le_{\text{H}_2} \sim 0.3$) led to superadiabatic surface temperatures, at least for modest heat transfer coefficients h . This is seen by the horizontal dashed lines marked T_{ad} ($= 1428.5 \text{ K}$) in Fig. 8, which denote the adiabatic equilibrium temperature of the incoming mixture ($\varphi=0.40$ and $T_{IN}=300 \text{ K}$). The higher wall temperatures at 1 bar compared to 5 bar are explained with the aid of Fig. 9 (referring to $k_s=16 \text{ Wm}^{-1}\text{K}^{-1}$), depicting streamwise profiles of the catalytic (C) and gaseous (G) hydrogen conversion rates and also of the wall temperatures T_{WALL} for the two pressures at three different h (Fig. 9(a1-f1)); the volumetric gaseous G rates have been integrated over the channel half-height b so as to be directly comparable to the surface catalytic rates C. Two-dimensional maps of the OH radical for all cases in Fig. 9(a1-f1) are provided in Fig. 9(a2-f2).

We have shown [38,40] that the presence of gaseous chemistry appreciably moderated the catalytically-induced superadiabatic wall temperatures by shielding the catalyst from the hydrogen-rich channel core. For $p=1$ bar, homogeneous ignition at $h=50 \text{ Wm}^{-2}\text{K}^{-1}$ was attained at $x \sim 7 \text{ mm}$ as manifested by the rise in the G profile of Fig. 9(a1). At $h=100 \text{ Wm}^{-2}\text{K}^{-1}$ gaseous combustion was very weak (see G profile in Fig. 9(b1)), while it practically vanished at $h=300 \text{ Wm}^{-1}\text{K}^{-1}$ (Fig. 9(c1)). The strong catalytic C conversion in Fig. 9(a1, b1, c1) caused in turn an appreciable superadiabatic T_{WALL} : peak wall temperatures exceeded

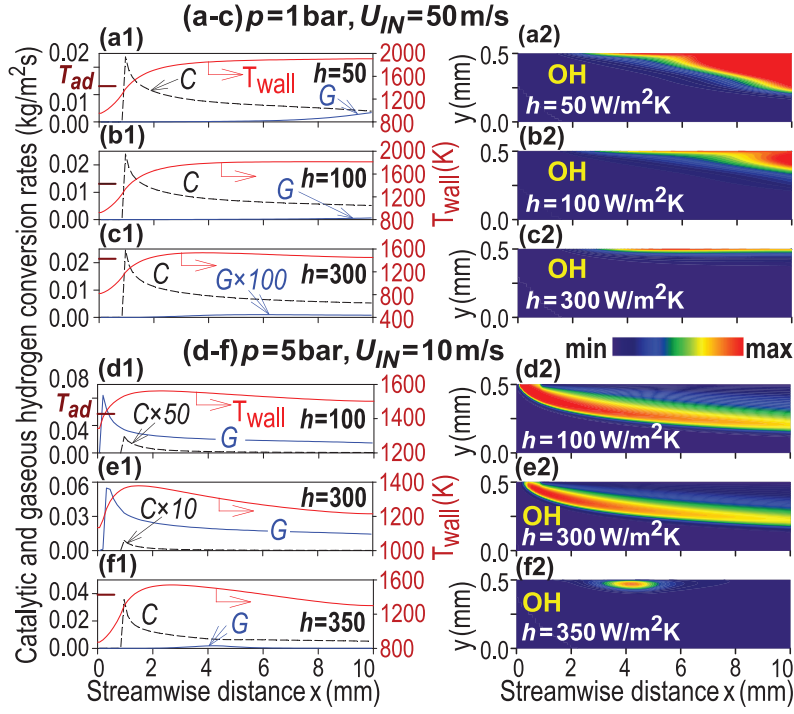


Fig. 9. Simulations for: (a-c) $p=1$ bar, $U_{IN}=50$ m/s, $k_s=16 \text{ Wm}^{-1}\text{K}^{-1}$, and (d-f) $p=5$ bar, $U_{IN}=10$ m/s, $k_s=16 \text{ Wm}^{-1}\text{K}^{-1}$ for various heat transfer coefficients h . (a1-f1): streamwise profiles of the catalytic (C) and gaseous (G) hydrogen conversion rates and of wall temperatures T_{WALL} . The horizontal ticks in the ordinates marked T_{ad} denote the adiabatic equilibrium temperature. (a2-f2): 2-D distributions of OH radical. In the provided color bar, the minimum OH is 0 and the maximum (ppm mass) is: (a2) 1.3×10^3 , (b2) 2.4×10^2 , (c2) 2.8×10^1 , (d2) 5.0×10^3 , (e2) 4.2×10^3 , (f2) 1.7×10^2 .

T_{ad} by 480, 388 and 106 K for $h=50$, 100 and 300 $\text{Wm}^{-1}\text{K}^{-1}$, respectively. On the other hand, at $p=5$ bar and for $h=100$ and 300 $\text{Wm}^{-2}\text{K}^{-1}$, flames were anchored close to the channel entry (in the catalytically-inert section of the channel, $0 \leq x < 1$ mm) and extended along the entire channel length as shown by the OH maps in Fig. 9(d2, e2), thus suppressing the catalytic conversion (see C profiles in Fig. 9(d1, e1)). The increasing importance of gaseous (G) combustion with rising pressure seen in Fig. 9(d1-f1) was demonstrated in Ghermay et al. [41]: they reported that even though the hydrogen gaseous reactivity had a complex non-monotonic dependence on pressure, for temperatures above 1200 K and modest pressures up to 5 bar, the gaseous reactivity increased monotonically with rising pressure.

Despite the strong gaseous combustion at $p=5$ bar and $h=100 \text{ Wm}^{-2}\text{K}^{-1}$, which led to a nearly complete suppression of catalytic conversion (see C plot in Fig. 9(d1)), superadiabatic temperatures were still attained (see Figs. 9(d1) or 8(d)) and the peak T_{WALL} exceeded T_{ad} by 132 K. This was due to another mechanism creating superadiabaticity (albeit considerably weaker than the catalytically-induced superadiabaticity discussed previously), namely the heat recirculation inside the solid wall that transferred heat upstream and preheated the reacting gas [68]. For a higher $h=300 \text{ Wm}^{-2}\text{K}^{-1}$ the wall temperatures were always underadiabatic (see Figs. 9(e1) or 8(d)). However, a further increase to $h=350 \text{ Wm}^{-2}\text{K}^{-1}$ led again to superadiabatic temperatures (the peak wall temperature exceeded T_{ad} by 112 K in Fig. 9(f1)) due to the nearly complete suppression of gaseous combustion and the re-emergence of the catalytically-induced superadiabaticity.

The attained peak wall temperatures were higher for $k_s=1 \text{ Wm}^{-1}\text{K}^{-1}$ compared to $k_s=16 \text{ Wm}^{-1}\text{K}^{-1}$, particularly at $p=5$ bar (see Fig. 8(b, d)). Streamwise profiles of the catalytic (C) and gaseous (G) hydrogen conversion rates and of the wall temperatures T_{WALL} are shown in Fig. 10(a1-d1) for $h=0$ and the two k_s . Upstream heat conduction in the wall was facilitated at higher

k_s , such that the wall temperatures over the inert section $0 \leq x < 1$ mm were higher for $k_s=16 \text{ Wm}^{-1}\text{K}^{-1}$ compared to $k_s=1 \text{ Wm}^{-1}\text{K}^{-1}$ as seen in Fig. 10(a1-d1). At $p=1$ bar homogeneous ignition was attained at $x \sim 5$ mm for both k_s (see G profiles in Fig. 10(a1, c1) and the OH maps in Fig. 10(a2, c2)), such that gaseous combustion was not appreciably affecting the catalytically-induced wall superadiabaticity in the upstream parts of the reactor. On the other hand, the higher gaseous reactivity at $p=5$ bar led to upstream homogeneous ignition positions. However, as the wall temperature was much higher at the channel entry for $k_s=16 \text{ Wm}^{-1}\text{K}^{-1}$ ($T_{WALL}=1397.7 \text{ K}$ at $x=0$) compared to $k_s=1 \text{ Wm}^{-1}\text{K}^{-1}$ ($T_{WALL}=380.3 \text{ K}$ at $x=0$), in the higher k_s the flame was anchored far-upstream ($x \sim 0.2$ mm) in the catalytically-inert channel section (see Fig. 10(d2)) thus completely suppressing the catalytic C conversion (see Fig. 10(d1)) and the catalytically-induced superadiabaticity. Conversely, for $k_s=1 \text{ Wm}^{-1}\text{K}^{-1}$ the flame anchored farther downstream ($x \sim 1.5$ mm, see Fig. 10(b2)), allowing for a significant catalytic (C) conversion over the length $x=1.0\text{--}1.5$ mm (see Fig. 10(b1)) and hence for an appreciable catalytically-induced superadiabaticity.

The interplay between catalytic kinetics, gaseous kinetics and transport was hence quite involved in the hetero-/homogeneous combustion of fuel-lean H₂/air mixtures, leading to the rich behaviors in Figs. 8–10. It is worth noting that gaseous combustion for the cases in Fig. 8 was significant only for modest external heat transfer coefficients (up to $h=100\text{--}150 \text{ Wm}^{-2}\text{K}^{-1}$ at $p=1$ bar and up to $h=350\text{--}500 \text{ Wm}^{-2}\text{K}^{-1}$ at $p=5$ bar). Close to extinction, whereby peak wall temperatures dropped down to 450 K (see Fig. 8) combustion was solely controlled by the catalytic reaction pathway. This was in contrast to hydrocarbons, where the stability limits of methane and propane in the same geometry of Fig. 1 were broadened by the presence of gaseous chemistry [29,48]. Nonetheless, for these hydrocarbon fuels the wall temperatures at extinction were considerably higher (800–1000 K).

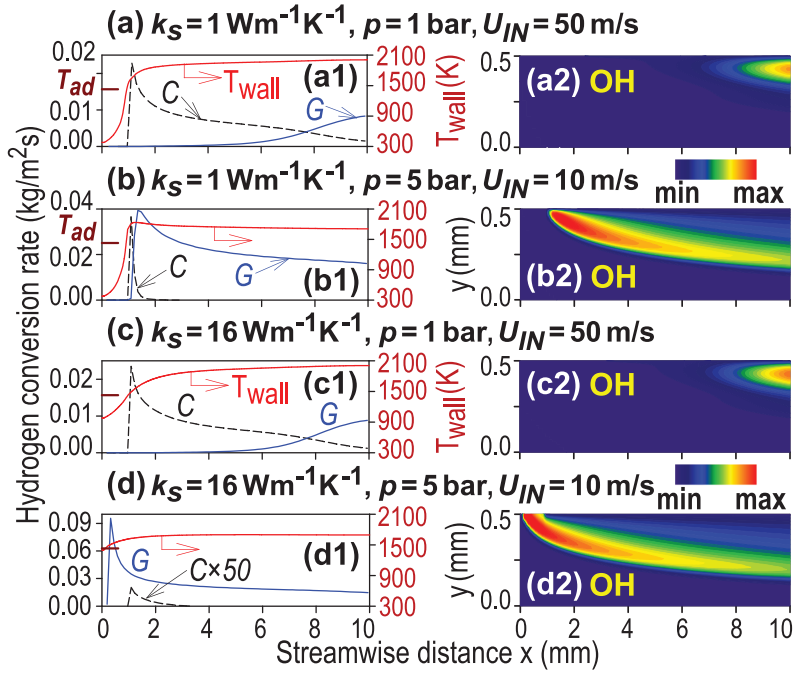


Fig. 10. Simulations for external heat transfer coefficient $h=0$ and: (a) $k_s = 1 \text{ Wm}^{-1}\text{K}^{-1}$, $p=1 \text{ bar}$, $U_{IN}=50 \text{ m/s}$, (b) $k_s = 1 \text{ Wm}^{-1}\text{K}^{-1}$, $p=5 \text{ bar}$, $U_{IN}=10 \text{ m/s}$, (c) $k_s = 16 \text{ Wm}^{-1}\text{K}^{-1}$, $p=1 \text{ bar}$, $U_{IN}=50 \text{ m/s}$, and (d) $k_s = 16 \text{ Wm}^{-1}\text{K}^{-1}$, $p=5 \text{ bar}$, $U_{IN}=10 \text{ m/s}$. (a1-d1): streamwise profiles of catalytic (C) and gaseous (G) hydrogen conversion rates and of wall temperatures. The horizontal ticks in the ordinates marked T_{ad} denote the adiabatic equilibrium temperature. (a2-d2): 2-D distributions of OH radical. In the provided color bar the minimum OH corresponds to 0 and the maximum (ppm mass) to: (a2) 4.0×10^3 , (b2) 5.6×10^3 , (c2) 4.3×10^3 , (d2) 6.2×10^3 .

3.2.2. Catalytic combustion at high heat transfer coefficients h

At high external heat transfer coefficients h , only heterogeneous combustion was present. Simulations for h close to h_{cr} (again for Region I of the stability maps and along line AB in Fig. 2), are illustrated in Fig. 11. The wall temperatures near extinction (already shown in Fig. 8) are repeated for clarity in Fig. 11(a1, b1), while the hydrogen catalytic conversion rates are plotted in Fig. 11(a2, b2). The wall temperatures exceeded $T_{IN}=T_\infty=300 \text{ K}$ only over narrow zones around the start of the catalytic section ($x=1 \text{ mm}$) for the low $k_s=1 \text{ Wm}^{-1}\text{K}^{-1}$ (Fig. 11(a1)), while for the higher $k_s=16 \text{ Wm}^{-1}\text{K}^{-1}$ the wall temperature distributions were broader (Fig. 11(b1)). It is worth noting that stable combustion was sustained even with peak wall temperatures as low as 453 K in Fig. 11(a1) and 481 K in Fig. 11(b1). The catalytic conversion rates C in Fig. 11(a2, b2) reached their peak immediately after the start of the catalytic section and then dropped sharply downstream due to the decreasing wall temperatures; nonetheless, the C rates still persisted at temperatures down to $\sim 380 \text{ K}$ (see Fig. 11(b1, b2)). Figure 11(a1, b1) further clarify the reason for the appreciably higher h_{cr} of the lower $k_s=1 \text{ Wm}^{-1}\text{K}^{-1}$ (see Fig. 2). The wall temperature profiles were significantly narrower for $k_s=1 \text{ Wm}^{-1}\text{K}^{-1}$ (compare Fig. 11(a1) and 11(b1)) such that lower solid thermal conductivity materials could tolerate much higher h_{cr} since only a small part of the channel surface contributed to the external heat losses $h(T_{WALL}-T_\infty)$ in Eq. (12). Apart from being more resilient to extinction, the lower solid thermal conductivity $k_s=1 \text{ Wm}^{-1}\text{K}^{-1}$ was also shown to facilitate catalytic ignition [66] due to the reduced amount of heat conducted away from the initial ignition hot spot. Finally, the obtained narrow wall temperature profiles in Fig. 11(a) resulted to much higher h_{cr} in the channel (Fig. 2) compared to the SPSR (Fig. 4(a)): even though both reactors had the same surface-to-volume ratio ($S/V=20 \text{ cm}^{-1}$), only a small fraction of the external channel surface area contributed to the heat loss $h(T_{WALL}-T_\infty)$ close to extinction and this allowed for much higher h_{cr} in the channel.

Surface coverages are finally provided in Fig. 11(a3, b3, a4, b4). Main coverages included Pt(s), H₂O(s) and OH(s) over the narrow channel lengths where C was appreciable. This was consistent with the coverages obtained for Region I of the SPSR in Fig. 6 (excluding the blowout SPSR branches in Region I, which were not accessible in the channel simulations). In the downstream parts of the channel where C dropped practically to zero, the dominant coverage was always H(s) indicating extinguished states.

Transverse profiles of hydrogen mass fractions at selected streamwise positions are plotted in Fig. 12 for the two pressures in Fig. 11(a1) with $k_s=1 \text{ Wm}^{-1}\text{K}^{-1}$. For $p=1 \text{ bar}$ in Fig. 12(a), the chemistry was slow at $x=1.5 \text{ mm}$ (corresponding to a high value of the wall-to-center hydrogen mass fraction ratio $Y_{H_2,W}/Y_{H_2,C}=0.86$), while it practically ceased at $x \geq 3.5 \text{ mm}$, as manifested by the nearly zero gradients of hydrogen at the wall $[\partial Y_{H_2}/\partial y]_{y=b} \sim 0$. The same trends were also observed at $p=5 \text{ bar}$ in Fig. 12(b), however, the surface chemistry at $x=1.5 \text{ mm}$ was now much faster as manifested by the appreciably lower ratio $Y_{H_2,W}/Y_{H_2,C}=0.032$.

The percentage hydrogen conversion is finally plotted in Fig. 13 for cases along line AB of Region I in Fig. 2. Conversions at $h=100 \text{ Wm}^{-2}\text{K}^{-1}$ ranged from 65% to 76% (5 bar) and 23% to 25% (1 bar), dropping to a few percent at extinction. For $p=1 \text{ bar}$ and for the last computed stable points before extinction, conversions were 1.2% at $k_s=1 \text{ Wm}^{-1}\text{K}^{-1}$ and 19.8% for $k_s=16 \text{ Wm}^{-1}\text{K}^{-1}$, while for 5 bar the conversion was 5.5% at $k_s=16 \text{ Wm}^{-1}\text{K}^{-1}$ (for $k_s=1 \text{ Wm}^{-1}\text{K}^{-1}$ no extinction was obtained up to the maximum investigated $h=10^5 \text{ Wm}^{-2}\text{K}^{-1}$).

3.3. Combustion stability in the microchannel at low velocities

The combustion stability for U_{IN} below the crossover points, marked as Region II in Fig. 2, is discussed in this section. Streamwise wall temperature profiles are plotted in Fig. 14 for the two pressures and two solid thermal conductivities and for various heat transfer coefficients h at $U_{IN}=1.5 \text{ m/s}$ ($p=1 \text{ bar}$) or 0.3 m/s

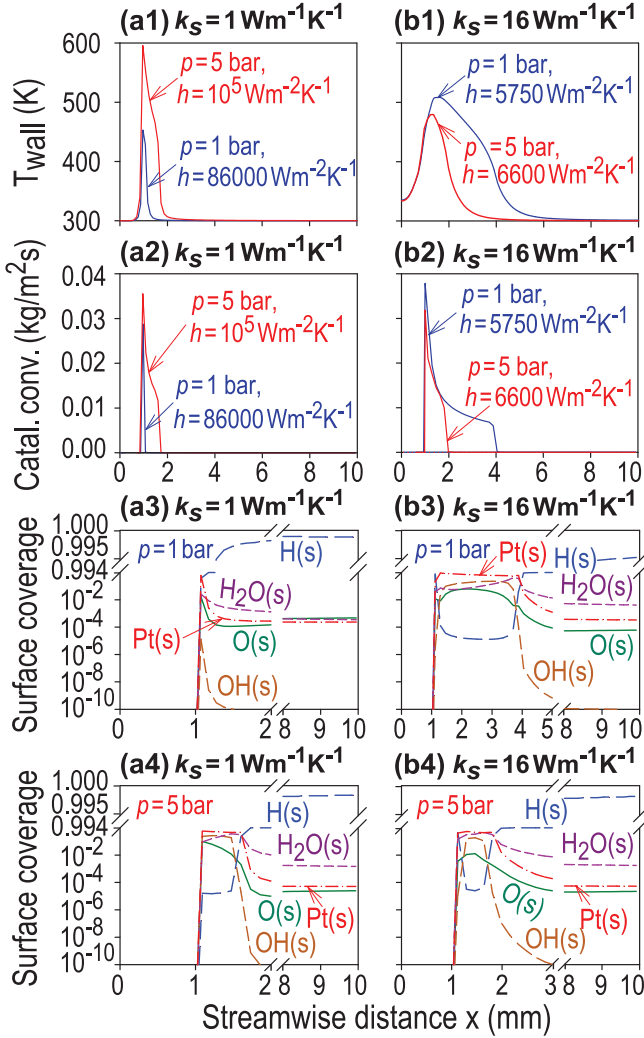


Fig. 11. Simulations for: (a1-a4) $k_s = 1 \text{ Wm}^{-1}\text{K}^{-1}$ and (b1-b4) $k_s = 16 \text{ Wm}^{-1}\text{K}^{-1}$, at heat transfer coefficients h close to the critical extinction coefficients h_{cr} . Other parameters are $U_{IN} = 50 \text{ m/s}$ ($p=1 \text{ bar}$) and $U_{IN} = 10 \text{ m/s}$ ($p=5 \text{ bar}$). All conditions fall along line AB in Fig. 2. Streamwise profiles of: (a1, b1) wall temperatures, (a2, b2) catalytic hydrogen conversion rates, (a3, b3) surface coverages at 1 bar, and (a4, b4) surface coverages at 5 bar.

($p=5 \text{ bar}$). The conditions in Fig. 14 fall along the line marked CD in Fig. 2. Heat transfer coefficients ranged from $h=0$ to values close to the critical heat transfer coefficient for extinction h_{cr} .

3.3.1. Combustion at low heat transfer coefficients h

At sufficiently low h , combined hetero-/homogeneous combustion occurred in the channel. The suppression of wall temperature superadiabaticity through gas-phase reactions (discussed in the foregoing Section 3.2.1) led to an anomalous behavior in Fig. 14(a) referring to $p=1 \text{ bar}$ and $k_s = 1 \text{ Wm}^{-1}\text{K}^{-1}$, whereby the peak wall temperature at $h=50 \text{ Wm}^{-2}\text{K}^{-1}$ was higher than the peak wall temperature at $h=0$. This is clarified with Fig. 15(a, b), providing the catalytic C and gas-phase G hydrogen conversion rates as well as the 2-D distributions of the OH radical and of the wall temperatures for the $h=0$ and $50 \text{ Wm}^{-2}\text{K}^{-1}$. Strong homogeneous combustion was attained at $h=0$ with the flame anchored close to $x \sim 0.1 \text{ mm}$ (see the G profile in Fig. 15(a1) and the OH map in Fig. 15(a2)), largely suppressing the C conversion (see C profile in Fig. 15(a1)). On the other hand, for $h=50 \text{ Wm}^{-2}\text{K}^{-1}$ homogeneous combustion was very weak and the catalytic conversion C dominated (see Fig. 15(b1)); this led in turn to a more

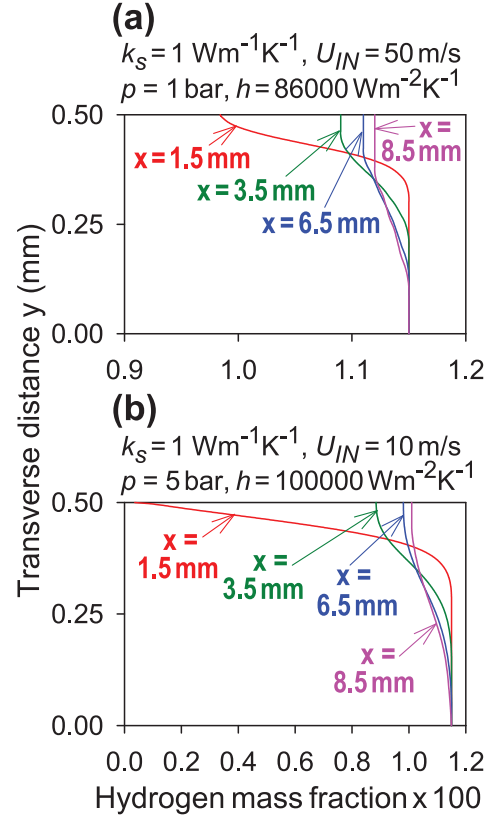


Fig. 12. Transverse profiles of hydrogen mass fraction: (a) $k_s = 1 \text{ Wm}^{-1}\text{K}^{-1}$, $p = 1 \text{ bar}$, $U_{IN} = 50 \text{ m/s}$, $h = 86,000 \text{ Wm}^{-2}\text{K}^{-1}$, and (b) $k_s = 1 \text{ Wm}^{-1}\text{K}^{-1}$, $p = 5 \text{ bar}$, $U_{IN} = 10 \text{ m/s}$, $h = 100,000 \text{ Wm}^{-2}\text{K}^{-1}$. The gas-wall interface is located at $y = 0.50 \text{ mm}$ and the channel center at $y = 0$.

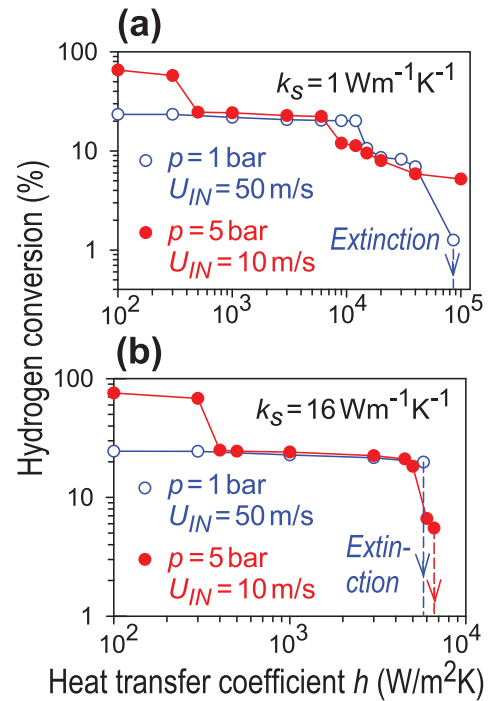


Fig. 13. Hydrogen conversion as a function of external heat transfer coefficient h : (a) $k_s = 1 \text{ Wm}^{-1}\text{K}^{-1}$, (b) $k_s = 16 \text{ Wm}^{-1}\text{K}^{-1}$. All points fall along line AB in Fig. 2.

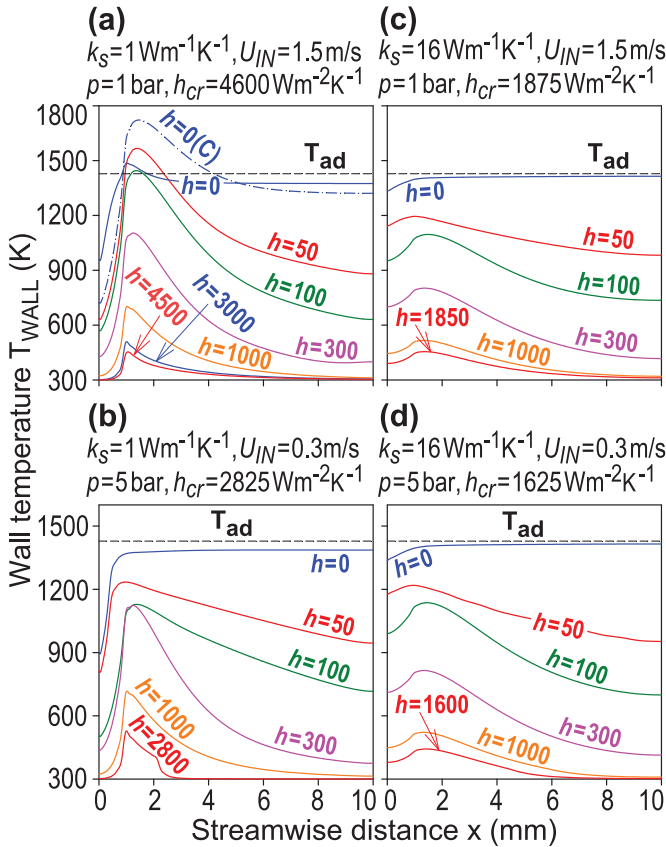


Fig. 14. Streamwise profiles of channel wall temperatures for various heat transfer coefficients h , ranging from 0 to values close to the critical h for extinction (h_{cr}). (a) $p=1$ bar, $U_{IN}=1.5$ m/s, $k_s=1$ Wm $^{-1}$ K $^{-1}$, (b) $p=5$ bar, $U_{IN}=0.3$ m/s, $k_s=1$ Wm $^{-1}$ K $^{-1}$, (c) $p=1$ bar, $U_{IN}=1.5$ m/s, $k_s=16$ Wm $^{-1}$ K $^{-1}$ and (d) $p=5$ bar, $U_{IN}=0.3$ m/s, $k_s=16$ Wm $^{-1}$ K $^{-1}$. Horizontal dashed lines marked T_{ad} denote the adiabatic equilibrium temperature (=1428.5 K).

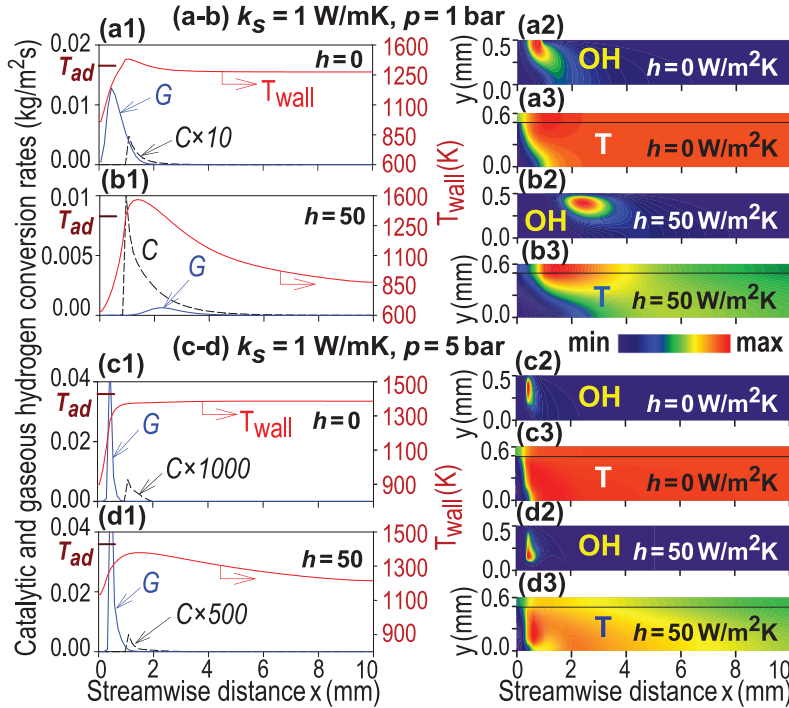


Fig. 15. Simulations for: (a, b) $p=1$ bar, $U_{IN}=1.5$ m/s, $k_s=1$ Wm $^{-1}$ K $^{-1}$, and (c, d) $p=5$ bar, $U_{IN}=0.3$ m/s, $k_s=1$ Wm $^{-1}$ K $^{-1}$. (a1-d1): streamwise profiles of the catalytic (C) and gaseous (G) hydrogen conversion rates and of wall temperatures T_{WALL} . The horizontal ticks in the ordinates marked T_{ad} denote the adiabatic equilibrium temperature. (a2-d2): 2-D distributions of the OH radical. (a3-d3): 2-D distributions of the temperature in the gas and solid. The black horizontal lines denote the gas-solid interfaces. In the provided color bar the minimum OH is 0 and the maximum (ppm mass) is: (a2) 3.6×10^3 , (b2) 3.5×10^2 , (c2) 2.7×10^3 , (d2) 3.2×10^3 . The minimum temperature is 300 K and the maximum is: (a3) 1482.7 K, (b3) 1567.2 K, (c3) 1498.5 K and (d3) 1588.9 K.

pronounced catalytically-induced surface superadiabaticity at $h=50$ Wm $^{-2}$ K $^{-1}$. To exemplify this effect, an additional simulation is shown in Fig. 14(a) for $h=0$ with catalytic chemistry alone (no gas-phase reactions), marked as $h=0$ (C); this simulation resulted in a higher peak wall temperature due to the lack of the temperature-moderating impact of gaseous combustion.

Simulations for $p=5$ bar and $k_s=1$ Wm $^{-1}$ K $^{-1}$ are shown in Fig. 15(c1-c3) and Fig. 15(d1-d3) referring to $h=0$ and 50 Wm $^{-2}$ K $^{-1}$, respectively. Strong gas-phase combustion was established at both $h=0$ and 50 Wm $^{-2}$ K $^{-1}$ (see G profiles in Fig. 15(c1, d1) and the OH maps in Fig. 15(c2, d2)). Wall temperatures in the low-velocity cases of Fig. 14 were ~ 300 K lower compared to the corresponding temperatures in the high-velocity cases of Fig. 8 at the same h , due to the lower chemical energy input of the former cases. The lower wall temperatures, in turn, led to the observed lower threshold values of h above which gaseous combustion was suppressed in Fig. 14 ($h=60$ -100 Wm $^{-2}$ K $^{-1}$ at $p=1$ bar and $h=100$ -150 Wm $^{-2}$ K $^{-1}$ at $p=5$ bar) compared to Fig. 8 (100-150 Wm $^{-2}$ K $^{-1}$ and 350-500 Wm $^{-2}$ K $^{-1}$, respectively). The 2-D temperature distributions inside the solid shown in Fig. 15(a3, b3, c3, d3) indicated that, for a given streamwise distance x , the maximum temperature differences across the 0.1 mm thick solid were modest, ranging from 24.9 K in Fig. 15(d3) to 37.7 K in Fig. 15(b3). Finally, the maximum temperatures for the 5 bar cases in Fig. 15(c3, d3) were attained in the gas and not at the gas-wall interface.

3.3.2. Combustion at modest-to-high heat transfer coefficients h

For heat transfer coefficients h exceeding 60-150 Wm $^{-2}$ K $^{-1}$ only heterogeneous combustion was active. Simulations along line CD in Fig. 2 for h close to extinction are illustrated in Fig. 16. Wall temperatures are depicted in Fig. 16(a1, b1) and hydrogen catalytic conversion rates in Fig. 16(a2, b2). There were key differences between the wall temperatures and catalytic conversions in Fig. 16(a1, b1) and Fig. 16(a2, b2) to the corresponding high-velocity plots in Fig. 11(a1, b1) and Fig. 11(a2, b2). Firstly, the axial

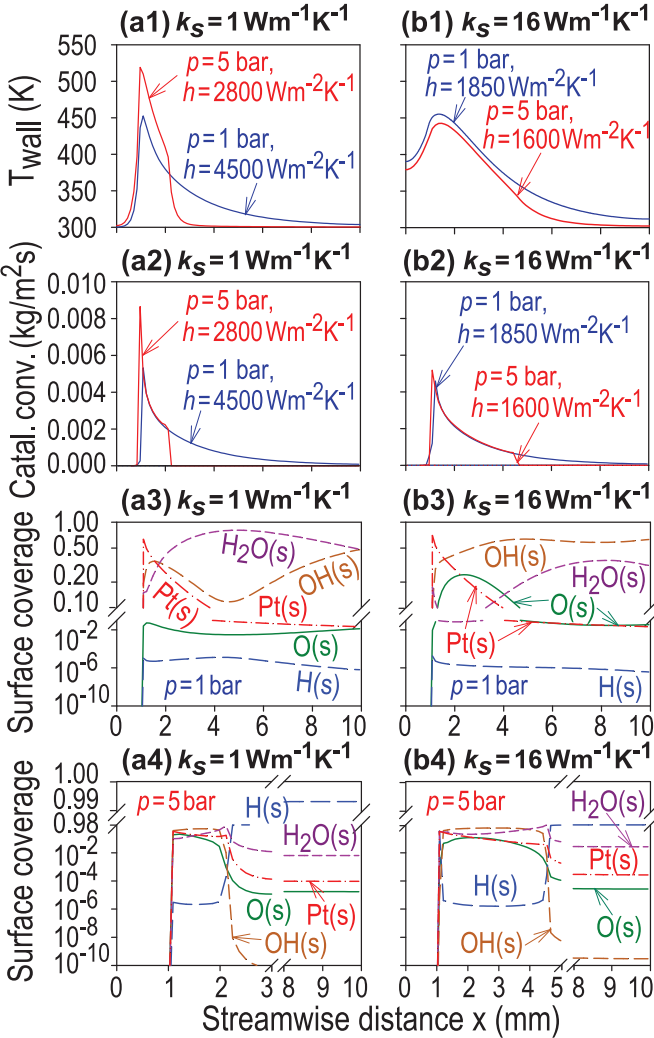


Fig. 16. Simulations for: (a1-a4) $k_s = 1 \text{ Wm}^{-1}\text{K}^{-1}$ and (b1-b4) $k_s = 16 \text{ Wm}^{-1}\text{K}^{-1}$, at heat transfer coefficients h close to the critical extinction coefficients h_{cr} . Other parameters are $U_{IN} = 1.5 \text{ m/s}$ ($p=1 \text{ bar}$) and $U_{IN} = 0.3 \text{ m/s}$ ($p=5 \text{ bar}$). All conditions fall along line CD in Fig. 2. Streamwise profiles of: (a1, b1) wall temperatures, (a2, b2) catalytic hydrogen conversion rates, (a3, b3) surface coverages at 1 bar, and (a4, b4) surface coverages at 5 bar.

extents of the low-velocity profiles were substantially broader than their high-velocity counterparts, particularly at $p=1 \text{ bar}$. Secondly, the peak wall temperatures of the low-velocity cases in Fig. 16(a1, b1) (443 to 519 K) were lower compared to the peak wall temperatures of the high-velocity cases in Fig. 11(a1, b1) (454 to 596 K). Both effects were a result of the appreciable catalytic conversions C at lower wall temperatures for the low velocity (i.e. high residence times) cases, especially at 1 bar (see Fig. 16(a2, b2) and compare to Fig. 11(a2, b2)). This was in agreement with the SPSR simulations in Fig. 4(b), which yielded lower reactor temperatures T_r at lower inverse residence times τ^{-1} .

The observed higher resilience to extinction of the 1 bar cases compared to the corresponding 5 bar cases below the crossover points was a result of the higher catalytic reactivity at 1 bar: for wall temperatures down to $\sim 320 \text{ K}$, the catalytic conversion persisted at 1 bar but practically vanished at 5 bar as shown in Fig. 16(a2, b2)). This behavior was also in agreement with the SPSR results in Fig. 4(a). Finally, there was an initial non-monotonic behavior of the h_{cr} versus U_{IN} stability plots in Fig. 2 for $k_s=1 \text{ Wm}^{-1}\text{K}^{-1}$, in agreement with the SPSR simulations (segments a_1b_1 and a_5b_5 in Fig. 4(a)). On the other hand, no such behavior was

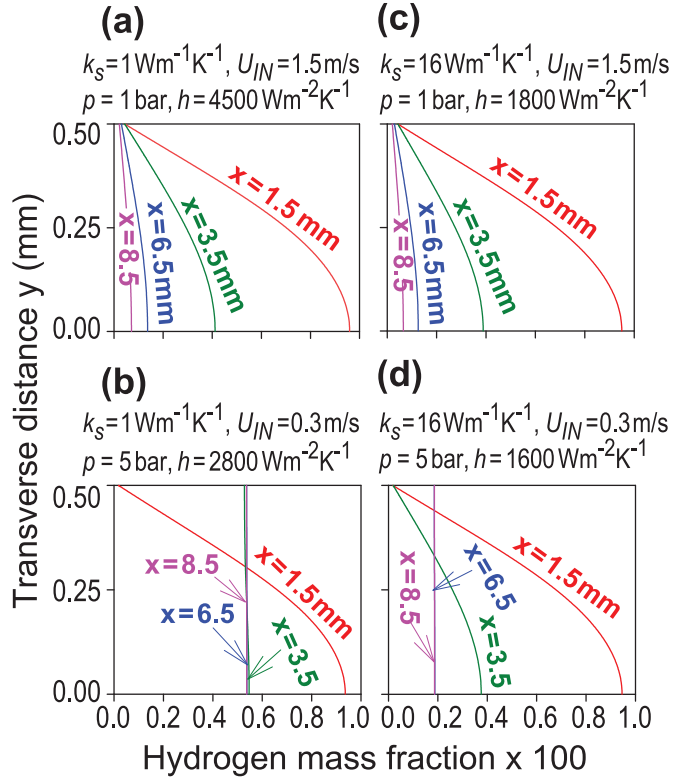


Fig. 17. Transverse profiles of hydrogen mass fraction: (a) $k_s = 1 \text{ Wm}^{-1}\text{K}^{-1}$, $p=1 \text{ bar}$, $U_{IN} = 1.5 \text{ m/s}$, $h=4500 \text{ Wm}^{-2}\text{K}^{-1}$, (b) $k_s = 1 \text{ Wm}^{-1}\text{K}^{-1}$, $p=5 \text{ bar}$, $U_{IN} = 0.3 \text{ m/s}$, $h=2800 \text{ Wm}^{-2}\text{K}^{-1}$, (c) $k_s = 16 \text{ Wm}^{-1}\text{K}^{-1}$, $p=1 \text{ bar}$, $U_{IN} = 1.5 \text{ m/s}$, $h=1850 \text{ Wm}^{-2}\text{K}^{-1}$, and (d) $k_s = 16 \text{ Wm}^{-1}\text{K}^{-1}$, $p=5 \text{ bar}$, $U_{IN}=0.3 \text{ m/s}$, $h=1600 \text{ Wm}^{-2}\text{K}^{-1}$. The gas-wall interface is located at $y=0.50 \text{ mm}$ and the channel center at $y=0$.

evident at $k_s = 16 \text{ Wm}^{-1}\text{K}^{-1}$ in Fig. 2 (it could be present, however, at velocities U_{IN} lower than the herein investigated ranges).

Surface coverages are shown in Fig. 16(a3, b3, a4, b4). Main coverages were OH(s), H₂O(s) and Pt(s) over the lengths whereby C was appreciable. Furthermore, the OH(s) and H₂O(s) coverages in the low velocity Region II of Fig. 16 were higher than Pt(s) whereas in the high velocity Region I of Fig. 11 Pt(s) was dominant. This was in accordance with the shift in main coverages between Regions I and II in the SPSR simulations of Fig. 6.

Transverse profiles of hydrogen mass fractions at selected streamwise positions are plotted in Fig. 17 for the four cases in Fig. 16(a1, b1). For $p=1 \text{ bar}$ in Fig. 17(a, c), the chemistry was fast down to $x=8.5 \text{ mm}$ (as manifested by the low values of the wall-to-center hydrogen mass fraction ratio $Y_{H_2,W}/Y_{H_2,C}$). For $p=5 \text{ bar}$ (Fig. 17(b, d)) the surface chemistry was fast at $x=1.5 \text{ mm}$ but it practically ceased at $x \geq 3.5 \text{ mm}$, as manifested by the nearly zero gradients of hydrogen at the wall [$\partial Y_{H_2}/\partial y|_{y=b} \sim 0$ (in agreement with the nearly zero C conversions in Fig. 16(a2, b2)) over this streamwise extent.

The percent hydrogen conversion along line CD in Fig. 2 is plotted in Fig. 18. For $h=100 \text{ Wm}^{-2}\text{K}^{-1}$ nearly complete conversions were attained, ranging from 98.9% to 100.0%. For the last computed stable points just before extinction, conversions at 5 bar were 51.7% for $k_s = 1 \text{ Wm}^{-1}\text{K}^{-1}$ and 82.9% for $k_s = 16 \text{ Wm}^{-1}\text{K}^{-1}$, while at 1 bar conversions were 96.2% for $k_s = 1 \text{ Wm}^{-1}\text{K}^{-1}$ and 96.5% at for $k_s = 16 \text{ Wm}^{-1}\text{K}^{-1}$. The conversions at the extinction points in Fig. 18 were substantially higher than the corresponding ones for the higher velocity studies in Fig. 13. This was again in qualitative agreement with the SPSR results in Fig. 4(b), whereby at low inverse residence times τ^{-1} the conversions at the critical extinction points were in the range 90–100%.

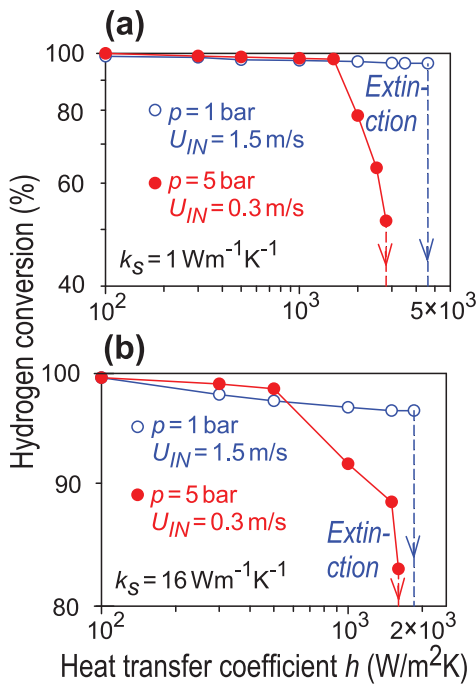


Fig. 18. Hydrogen conversion as a function of external heat transfer coefficient h : (a) $k_s = 1 \text{ Wm}^{-1}\text{K}^{-1}$, (b) $k_s = 16 \text{ Wm}^{-1}\text{K}^{-1}$. All points fall along line CD in Fig. 2.

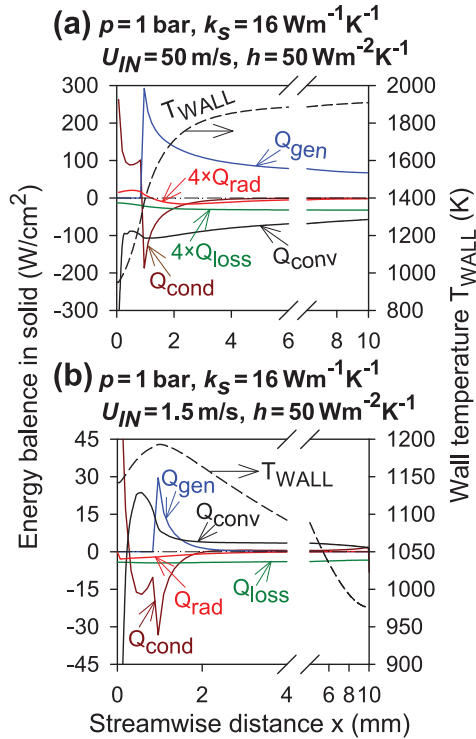


Fig. 19. Axial profiles of energy balances in the solid for $p = 1 \text{ bar}$, $k_s = 16 \text{ Wm}^{-1}\text{K}^{-1}$, $h = 50 \text{ Wm}^{-2}\text{K}^{-1}$: (a) $U_{IN} = 50 \text{ m/s}$, and (b) $U_{IN} = 1.5 \text{ m/s}$. The wall temperatures, T_{WALL} , are also shown.

Finally, the effect of surface radiation heat transfer is discussed. The energy balance for each differential solid element (length Δx and thickness δ_s) is illustrated in Fig. 19 for two cases with a modest $h = 50 \text{ Wm}^{-2}\text{K}^{-1}$ and two velocities, $U_{IN} = 50$ and 1.5 m/s . Therein, Q_{cond} denoted the y -integrated (over the twenty transverse solid volumes) heat conduction, Q_{gen} the chemical heat release due to catalytic reactions, Q_{conv} the convective heat loss to the gas, Q_{rad}

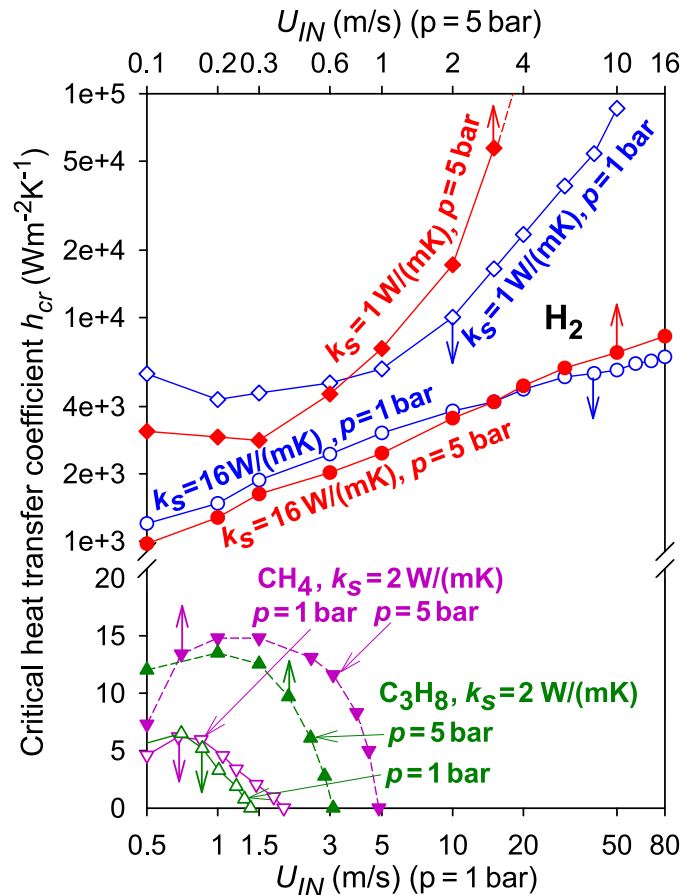


Fig. 20. Stability diagrams for H_2/air (diamonds and circles) and for CH_4/air (lower triangles) and $\text{C}_3\text{H}_8/\text{air}$ (upper triangles) in the channel geometry of Fig. 1. In all fuels $\varphi = 0.40$, with the methane and propane data referring to [48]. Open symbols are 1 bar and filled symbols 5 bar .

the radiation heat transfer on the catalytic surface, and Q_{loss} the heat losses due to the external heat transfer coefficient h ; all terms in Fig. 19 have been referenced to the area of each differential catalytic surface element.

The magnitude of the radiation term Q_{rad} was lower than that of the heat loss Q_{loss} for both cases in Fig. 19. Nonetheless, radiation was not altogether unimportant. Simulations were repeated for the two cases in Fig. 19, without inclusion of surface radiation heat transfer. Simulations with surface radiation heat transfer always yielded lower wall temperatures than those without radiation heat transfer, due to the heat losses towards the colder (300 K) entry enclosure. Specifically, for the higher mass throughput case in Fig. 19(a) the two simulations differed by a maximum of 14 K; however, for the lower mass throughput in Fig. 19(b) the wall temperature differences were appreciable, reaching up to 38 K. Finally, near the stability limits radiation was altogether insignificant as the wall temperatures were too low ($\sim 450 \text{ K}$).

3.4. Comparisons with stability limits of hydrocarbons

Stability diagrams of hydrogen and of methane and propane hetero-/homogeneous combustion over platinum in the channel geometry of Fig. 1 are compared in Fig. 20. The methane and propane data were reported in Karagiannidis et al. [48], and referred also to $\varphi = 0.40$ mixtures, however, with inlet temperatures $T_{IN} = 700 \text{ K}$ and a solid thermal conductivity $k_s = 2 \text{ Wm}^{-1}\text{K}^{-1}$.

Hydrogen had much broader combustion stability envelopes compared to either methane or propane. In particular, while

blowout limits for methane and propane were reached at modest inlet velocities up to 1.9 m/s and 1.4 m/s at 1 bar, respectively (up to 0.97 m/s and 0.62 m/s at 5 bar), hydrogen was resilient against blowout even at inlet velocities as high as 80 m/s (1 bar) or 16 m/s (5 bar). Moreover, when considering mass throughputs rather than inlet velocities in Fig. 20, methane and propane had even narrower stability envelopes than hydrogen. This was due to the high preheat ($T_{IN} = 700$ K) in methane and propane that resulted in mass throughputs more than a factor of two lower than those of hydrogen ($T_{IN} = 300$ K). In addition, contrary to hydrogen, the methane and propane fuels did not exhibit crossover points in their stability plots.

Critical extinction heat transfer coefficients h_{cr} for hydrogen were orders of magnitude larger than the corresponding ones for methane and propane, due to the ability of hydrogen to sustain stable combustion at wall temperatures down to ~ 380 K at high velocities and ~ 320 K at low velocities. This property of hydrogen was highly desirable in many practical applications. For example, we have investigated a combined combustion/solar microreactor for power generation [14], aiming at an increased annual capacity factor (ratio of yearly production of energy to the theoretically maximum yearly energy output). Therein, combustion of hydrogen in catalytic channels supplemented the solar power input (when the latter fell below a certain limit) by adjusting the chemical energy input in the microreactor so as to maintain a constant power level. The present study has shown that this hybrid system could tolerate sudden drops of solar power (or even complete loss of solar power) since, during the transient period required to substitute a rapidly dropping solar power input with chemical power, the risk of extinction is minimized.

Finally, future studies should investigate the stability limits of syngas fuels, due to their increasing importance in current power generation systems and also due to the intricate catalytic chemistry coupling between H₂ and CO [53]; moreover, extension of the present studies to pressures up to 15 bar relevant to large-scale gas turbines is desirable.

4. Conclusions

The hetero-/homogeneous combustion characteristics and the stability limits of a fuel-lean (equivalence ratio $\varphi = 0.40$) H₂/air mixture were investigated numerically in a planar channel with a length of 10 mm, out of which 9 mm were coated with platinum, and a height of 1 mm. Two-dimensional simulations were carried out for both the gas-phase and the 0.1-mm-thick solid wall, using elementary heterogeneous and homogeneous chemical reaction mechanisms, detailed transport, surface radiation heat transfer, solid heat conduction, and external losses via a heat transfer coefficient h . Pressures of 1 and 5 bar and solid thermal conductivities $k_s = 1$ and 16 Wm⁻¹K⁻¹ (pertaining to cordierite and FeCr-alloy materials, respectively) were studied, with parametric variation of the inlet velocity U_{IN} and heat transfer coefficient h . Critical extinction coefficients h_{cr} were determined by one-parameter continuation. The following are the key conclusions of this study:

- (1) Stability plots constructed in the critical extinction heat transfer coefficient h_{cr} versus inlet velocity U_{IN} (or mass throughput) parameter space revealed that, for a given solid thermal conductivity k_s , there existed crossover points, whereby above a specific mass throughput the stability envelopes were broader at 5 bar while below it the stability envelopes were broader at 1 bar. Additional simulations and construction of stability maps using a simpler surface perfectly stirred reactor (SPSR) model, qualitatively reproduced the aforementioned crossover points, which were attributed

to a shift in the pressure-dependence of the catalytic reactivity of hydrogen on platinum.

- (2) For the lower solid thermal conductivity $k_s = 1$ Wm⁻¹K⁻¹, a non-monotonic dependence of the stability limits on mass throughput was shown, with a local minimum appearing at a location below the crossover point. SPSR model simulations have also captured this behavior, which was a result of hydrogen's capacity to sustain stable catalytic combustion at the continuously diminishing temperatures with dropping mass throughputs. This in turn allowed the reactor to tolerate increasingly higher external heat transfer coefficients h with dropping mass throughputs.
- (3) The lower solid thermal conductivity material, $k_s = 1$ Wm⁻¹K⁻¹, yielded substantially wider stability envelopes compared to $k_s = 16$ Wm⁻¹K⁻¹, irrespective of pressure. This was due to the creation of localized hot spots on the channel, in which combustion could be sustained without detrimental loss of thermal energy via excessive heat conduction in the solid.
- (4) Blowout limits could not be reached even for inlet velocities as high as 80 m/s at 1 bar (or 16 m/s at 5 bar). This was in contrast to previous hetero-/homogeneous combustion stability studies of methane and propane, which exhibited modest blowout velocities (up to ~ 2 m/s at 1 bar and ~ 1 m/s at 5 bar). Moreover, while the presence of homogeneous combustion extended the stability limits of methane and propane, the stability limits of hydrogen were solely determined by catalytic chemistry due to its capacity to sustain stable combustion at temperatures as low as 320–380 K at which gas-phase chemistry was frozen.
- (5) Away from the critical extinction points and for heat transfer coefficients below the range $h=100\text{--}500$ Wm⁻²K⁻¹ at high mass throughputs and 60–150 Wm⁻²K⁻¹ at low mass throughputs, combustion was controlled by both the catalytic and gas-phase reaction pathways. The diffusional imbalance of hydrogen that led to catalytically-induced superadiabatic surface temperatures and the suppression of this superadiabaticity by the presence of gaseous chemistry led to rich combustion phenomena. For example, the peak temperatures at the gas-wall interface could, under certain conditions, increase with increasing external heat transfer coefficients h .
- (6) SPSR simulations have shown that at sufficiently long residence times (equivalent to low mass throughputs) most of the surface was covered by H₂O(s) such that an increase in hydrogen adsorption rendered combustion more resilient to extinction. At the blowout limits, however, hydrogen coverage was significant and an increase of oxygen adsorption stabilized combustion. Thus, while the lack of hydrogen controlled extinction over most residence times, at the blowout limits (very short residence times) the dominant extinction mechanism was lack of surface oxygen. This behavior was qualitatively similar to that observed in the channel reactor (apart from the blowout, which was not attainable in the channel).
- (7) Hydrogen conversions at extinction were low at high mass throughputs in the channel (a few percent), while at low mass throughputs conversions in excess of 50% were obtained.
- (8) Critical heat transfer coefficients for hydrogen were, for a given mass throughput, three to four orders of magnitude higher than those of methane and propane fuels. This was highly desirable in many practical systems, such as hybrid solar/catalytic-combustion microreactor applications, where the resilience of hydrogen to extinction allowed for flexibility in the temporal control of the percentages of the

combustion and solar power inputs. Finally, surface radiation heat transfer was appreciable for low external heat transfer coefficients and low velocities and it resulted in a drop of the wall temperatures by ~40 K due to heat losses towards the cold inlet.

Acknowledgments

Support was provided by the European Union project Hybrid Renewable energy Converter for continuous and flexible power production (HRC-Power).

References

- [1] E.S. Rubin, H. Mantripragada, A. Marks, P. Versteeg, J. Kitchin, The outlook for improved carbon capture technology, *Prog. Energy Combust. Sci.* 38 (2012) 630–671.
- [2] A.M. Elkady, A. Evulet, A. Brand, T.P. Ursin, A. Lynghjem, Application of exhaust gas recirculation in a DLN F-class combustion system for postcombustion carbon capture, *ASME GT2008-51152*, 2008.
- [3] A. Schneider, J. Mantzaras, R. Bombach, S. Schenker, N. Tylli, P. Jansohn, Laser induced fluorescence of formaldehyde and Raman measurements of major species during partial catalytic oxidation of methane with large H_2O and CO_2 dilution at pressures up to 10 bar, *Proc. Combust. Inst.* 31 (2007) 1973–1981.
- [4] D. Winkler, P. Mueller, S. Reimer, T. Griffin, A. Burdet, J. Mantzaras, Y. Ghermay, Improvement of gas turbine combustion reactivity under flue gas recirculation condition with in situ hydrogen addition, *ASME GT2009-59182*, 2009.
- [5] M. Gambini, M. Veillini, Natural gas decarbonization technologies for advanced power plants, *J. Eng. Gas Turb. Power* 129 (2006) 1114–1124.
- [6] S. Hoffmann, M. Bartlett, M. Finkenrath, A. Evulet, T.P. Ursin, Performance and cost analysis of advanced gas turbine cycles with precombustion CO_2 capture, *ASME GT2008-51027*, 2008.
- [7] J.D. Figueroa, T. Fout, S. Plasynski, H. McIlvried, R.D. Srivastava, Advances in CO_2 capture technology - US department of energy's carbon sequestration program, *Int. J. Greenh. Gas. Control* 2 (2008) 9–20.
- [8] A. Keromines, W.K. Metcalfe, K.A. Haufer, N. Donohoe, A.K. Das, C.-J. Sung, J. Herzler, C. Naumann, P. Griebel, O. Mathieu, M.C. Krejci, E.L. Petersen, W.J. Pitz, H.J. Curran, An experimental and detailed chemical kinetic modeling study of hydrogen and syngas mixture oxidation at elevated pressures, *Combust. Flame* 160 (2013) 995–1011.
- [9] M. Goswami, R. Bastiaans, A.A. Konnov, L.P.H. de Goye, Laminar burning velocity of lean H_2 - CO mixtures at elevated pressure using the heat flux method, *Int. J. Hydrogen Energy* 39 (2014) 1485–1498.
- [10] Y. Ghermay, J. Mantzaras, R. Bombach, Experimental and numerical investigation of hetero-/homogeneous combustion of $CO/H_2/O_2/N_2$ mixtures over platinum at pressures up to 5 bar, *Proc. Combust. Inst.* 33 (2011) 1827–1835.
- [11] D.G. Norton, E.D. Wetzel, D.G. Vlachos, Fabrication of single-channel catalytic microburners: effect of confinement on the oxidation of hydrogen/air mixtures, *Ind. Eng. Chem. Res.* 43 (2004) 4833–4840.
- [12] S. Karagiannidis, J. Mantzaras, Numerical investigation on the hydrogen-assisted start-up of methane-fueled, catalytic microreactors, *Flow Turbul. Combust.* 89 (2012) 215–230.
- [13] V.B. Svetovoy, R.G.P. Sanders, K.C. Ma, M.C. Elwenspoek, New type of micro-engine using internal combustion of hydrogen and oxygen, *Sci. Rep.* 4 (2014) 4296.
- [14] R. Sui, N.I. Prasianakis, J. Mantzaras, N. Mallya, J. Theile, D. Lagrange, M. Friess, An experimental and numerical investigation of the combustion and heat transfer characteristics of hydrogen-fueled catalytic microreactors, *Chem. Eng. Sci.* 141 (2016) 214–230.
- [15] J.D. Holladay, Y. Wang, E. Jones, Review of developments in portable hydrogen production using microreactor technology, *Chem. Rev.* 104 (2004) 4767–4789.
- [16] C.M. Balonok, J.L. Colby, L.D. Schmidt, Millisecond catalytic reforming of monoaromatics over noble metals, *AIChE J.* 56 (2010) 979–988.
- [17] B. Jiang, A.J. Santis-Alvarez, P. Muralt, D. Poulikakos, N. Bohrani, J.R. Thome, T. Maeder, Design and packaging of a highly integrated microreactor system for high-temperature on-board hydrogen production, *Chem. Eng. J.* 275 (2015) 206–219.
- [18] R. Carroni, T. Griffin, Catalytic hybrid lean combustion for gas turbines, *Catal. Today* 155 (2010) 2–12.
- [19] W.C. Pfefferle, L.D. Pfefferle, Catalytically stabilized combustion, *Prog. Energy Combust. Sci.* 12 (1986) 25–41.
- [20] J. Mantzaras, C. Appel, Effects of finite rate heterogeneous kinetics on homogeneous ignition in catalytically stabilized channel-flow combustion, *Combust. Flame* 130 (2002) 336–351.
- [21] G. Pizza, C.E. Frouzakis, J. Mantzaras, A.G. Tomboulides, K. Boulouchos, Dynamics of premixed hydrogen/air flames in mesoscale channels, *Combust. Flame* 155 (2008) 2–20.
- [22] G. Pizza, C.E. Frouzakis, J. Mantzaras, A.G. Tomboulides, K. Boulouchos, Three-dimensional simulations of premixed hydrogen/air flames in microtubes, *J. Fluid Mech.* 658 (2010) 463–491.
- [23] C.J. Evans, D.C. Kyritsis, Operational regimes of rich methane and propane/oxygen flames in mesoscale non-adiabatic ducts, *Proc. Combust. Inst.* 32 (2009) 3107–3114.
- [24] A.W. Fan, J.L. Wan, K. Maruta, H. Nakamura, H. Yao, W. Liu, Flame dynamics in a heated meso-scale radial channel, *Proc. Combust. Inst.* 34 (2013) 3351–3359.
- [25] A. Brambilla, M. Schultze, C.E. Frouzakis, J. Mantzaras, R. Bombach, K. Boulouchos, An experimental and numerical investigation of premixed syngas combustion dynamics in mesoscale channels with controlled wall temperature profiles, *Proc. Combust. Inst.* 35 (2015) 3429–3437.
- [26] G. Pizza, J. Mantzaras, C.E. Frouzakis, A.G. Tomboulides, K. Boulouchos, Suppression of combustion instabilities of premixed hydrogen/air flames in microchannels using heterogeneous reactions, *Proc. Combust. Inst.* 32 (2009) 3051–3058.
- [27] G. Pizza, J. Mantzaras, C.E. Frouzakis, Flame dynamics in catalytic and non-catalytic mesoscale microreactors, *Catal. Today* 155 (2010) 123–130.
- [28] D.G. Norton, D.G. Vlachos, Combustion characteristics and flame stability at the microscale: a CFD study of premixed methane/air mixtures, *Chem. Eng. Sci.* 58 (2003) 4871–4882.
- [29] S. Karagiannidis, J. Mantzaras, G. Jackson, K. Boulouchos, Hetero-/homogeneous combustion and stability maps in methane-fueled microreactors, *Proc. Combust. Inst.* 31 (2007) 3309–3317.
- [30] J. Li, Z. Zhao, A. Kazakov, F.L. Dryer, An updated comprehensive kinetic model of hydrogen combustion, *Int. J. Chem. Kinet.* 36 (2004) 566–575.
- [31] M.P. Burke, M. Chaos, Y. Ju, F. Dryer, S.J. Klippenstein, Comprehensive H_2/O_2 kinetic model for high-pressure combustion, *Int. J. Chem. Kinet.* 44 (2012) 444–474.
- [32] C. Olm, I.G. Zsely, R. Pavolgyi, T. Varga, T. Nagy, H.J. Curran, T. Turanyi, Comparison of the performance of several recent hydrogen combustion mechanisms, *Combust. Flame* 161 (2014) 2219–2234.
- [33] O. Deutschmann, R. Schmidt, F. Behrendt, J. Warnatz, Numerical modeling of catalytic ignition, *Proc. Combust. Inst.* 26 (1996) 1747–1754.
- [34] M. Rinnemo, O. Deutschmann, F. Behrendt, B. Kasemo, Experimental and numerical investigation of the catalytic ignition of mixtures of hydrogen and oxygen on platinum, *Combust. Flame* 111 (1997) 312–326.
- [35] B. Hellsing, B. Kasemo, V.P. Zhdanov, Kinetics of the hydrogen oxygen reaction on platinum, *J. Catal.* 132 (1991) 210–228.
- [36] O. Deutschmann, L.I. Maier, U. Riedel, A.H. Stroemman, R.W. Dibble, Hydrogen assisted catalytic combustion of methane on platinum, *Catal. Today* 59 (2000) 141–150.
- [37] Y.K. Park, P. Aghalayam, D.G. Vlachos, A generalized approach for predicting coverage-dependent reaction parameters of complex surface reactions: application to H_2 oxidation over platinum, *J. Phys. Chem. A* 103 (1999) 8101–8107.
- [38] C. Appel, J. Mantzaras, R. Schaeren, R. Bombach, A. Inauen, B. Kaepeli, B. Hemmerling, A. Stampponi, An experimental and numerical investigation of homogeneous ignition in catalytically stabilized combustion of hydrogen/air mixtures over platinum, *Combust. Flame* 128 (2002) 340–368.
- [39] J. Mantzaras, R. Bombach, R. Schaeren, Hetero-/homogeneous combustion of hydrogen/air mixtures over platinum at pressures up to 10 bar, *Proc. Combust. Inst.* 32 (2009) 1937–1945.
- [40] Y. Ghermay, J. Mantzaras, R. Bombach, Effects of hydrogen preconversion on the homogeneous ignition of fuel-lean $H_2/O_2/N_2/CO_2$ mixtures over platinum at moderate pressures, *Combust. Flame* 157 (2010) 1942–1958.
- [41] Y. Ghermay, J. Mantzaras, R. Bombach, K. Boulouchos, Homogeneous combustion of fuel lean $H_2/O_2/N_2$ mixtures over platinum at elevated pressures and preheats, *Combust. Flame* 158 (2011) 1491–1506.
- [42] M. Schultze, J. Mantzaras, R. Bombach, K. Boulouchos, An experimental and numerical investigation of the hetero-/homogeneous combustion of fuel-rich hydrogen/air mixtures over platinum, *Proc. Combust. Inst.* 34 (2013) 2269–2277.
- [43] P.A. Bui, D.G. Vlachos, P.R. Westmoreland, Homogeneous ignition of hydrogen/air mixtures over platinum, *Proc. Combust. Inst.* 26 (1996) 1763–1770.
- [44] A. Brambilla, C.E. Frouzakis, J. Mantzaras, A. Tomboulides, S. Kerkemeier, K. Boulouchos, Detailed transient numerical simulation of H_2 /air hetero-/homogeneous combustion in platinum-coated channels with conjugate heat transfer, *Combust. Flame* 161 (2014) 2692–2707.
- [45] D.G. Norton, D.G. Vlachos, A CFD study of propane/air microflame stability, *Combust. Flame* 138 (2004) 97–107.
- [46] K. Maruta, K. Takeda, J. Ahn, K. Borer, L. Sitzki, P.D. Ronney, O. Deutschmann, Extinction limits of catalytic combustion in microchannels, *Proc. Combust. Inst.* 29 (2002) 957–963.
- [47] J.M. Ahn, C. Eastwood, L. Sitzki, P.D. Ronney, Gas-phase and catalytic combustion in heat-recirculating burners, *Proc. Combust. Inst.* 30 (2005) 2463–2472.
- [48] S. Karagiannidis, J. Mantzaras, K. Boulouchos, Stability of hetero-/homogeneous combustion in propane and methane fueled catalytic microreactors: channel confinement and molecular transport effects, *Proc. Combust. Inst.* 33 (2011) 3241–3249.
- [49] F. Behrendt, O. Deutschmann, R. Schmidt, J. Warnatz, Ignition and extinction of hydrogen-Air and methane-air mixtures over platinum and palladium, in: B. Warren (Ed.), *Heterogeneous Hydrocarbon Oxidation*, ACS Symposium Series, Washington DC (1996).
- [50] D.G. Vlachos, P.A. Bui, Catalytic ignition and extinction of hydrogen: comparison of simulations and experiments, *Surf. Sci.* 364 (1996) 1625–1630.
- [51] X. Zheng, J. Mantzaras, An analytical and numerical investigation of hetero-/homogeneous combustion with deficient reactants having larger than unity Lewis numbers, *Combust. Flame* 161 (2014) 1911–1922.
- [52] G.A. Boyarko, C.-J. Sung, S.J. Schneider, Catalyzed combustion of hydrogen-oxygen in platinum tubes for micro-propulsion applications, *Proc. Combust. Inst.* 30 (2005) 2481–2488.

- [53] X. Zheng, J. Mantzaras, R. Bombach, Kinetic interactions between hydrogen and carbon monoxide oxidation over platinum, *Combust. Flame* 161 (2014) 332–346.
- [54] B. Schneider, S. Karagiannidis, M. Bruderer, D. Dyntar, C. Zwysig, Q. Guangchun, M. Diener, K. Boulouchos, R.S. Abhari, L. Guzzella, J.W. Kolar, Ultra-high-energy-density converter for portable power, *Power-MEMS 2005*, Tokyo, Japan, November 28–30, 2005.
- [55] R. Siegel, J.R. Howell, *Thermal radiation heat transfer*, 271, Hemisphere, New York, 1981.
- [56] R.J. Kee, G. Dixon-Lewis, J. Warnatz, M.E. Coltrin, J.A. Miller, A Fortran computer code package for the evaluation of gas-phase multicomponent transport properties, Sandia National Laboratories, 1996 Report No. SAND86-8246.
- [57] S. Eriksson, A. Schneider, J. Mantzaras, M. Wolf, S. Jaras, Experimental and numerical investigation of supported rhodium catalysts for partial oxidation of methane in exhaust gas diluted reaction mixtures, *Chem. Eng. Sci.* 62 (2007) 3991–4011.
- [58] U. Dogwiler, P. Benz, J. Mantzaras, Two-dimensional modelling for catalytically stabilized combustion of a lean methane-air mixture with elementary homogeneous and heterogeneous chemical reactions, *Combust. Flame* 116 (1999) 243–258.
- [59] S. Karagiannidis, J. Mantzaras, Numerical investigation on the start-up of methane-fueled catalytic microreactors, *Combust. Flame* 157 (2010) 1400–1413.
- [60] A. Di Benedetto, V. Di Sarli, G. Russo, Effect of geometry on the thermal behavior of catalytic micro-combustors, *Catal. Today* 155 (2010) 116–122.
- [61] M. Hettel, C. Diehm, H. Bonart, O. Deutschmann, Numerical simulation of a structured catalytic methane reformer by DUO: the new computational interface for OpenFOAM and DETCHEM, *Catal. Today* 258 (2015) 230–240.
- [62] J. Warnatz, M.D. Allendorf, R.J. Kee, M.E. Coltrin, A model of elementary chemistry and fluid mechanics in the combustion of hydrogen on platinum surfaces, *Combust. Flame* 96 (1994) 393–406.
- [63] M.E. Coltrin, R.J. Kee, F.M. Rupley, Surface Chemkin, A Fortran package for analyzing heterogeneous chemical kinetics at the solid surface-gas phase interface, Sandia National Laboratories, 1996 Report No. SAND90-8003C.
- [64] R.J. Kee, F.M. Rupley, J.A. Miller, A Fortran chemical kinetics package for the analysis of gas-phase chemical kinetics, Sandia National Laboratories, 1996 Report No. SAND89-8009B.
- [65] A. Schneider, J. Mantzaras, S. Eriksson, Ignition and extinction in catalytic partial oxidation of methane-oxygen mixtures with large H_2O and CO_2 dilution, *Combust. Sci. Technol.* 180 (2008) 89–126.
- [66] N. Michelon, J. Mantzaras, P. Canu, Transient simulation of the combustion of fuel-lean hydrogen/air mixtures in platinum-coated channels, *Combust. Theory Model.* 19 (2015) 514–548.
- [67] H.K. Moffat, R.J. Kee, J.F. Grcar, J.A. Miller, Surface PSR: A Fortran program for modeling well-stirred reactors with gas and surface reactions, 1993. Report No. SAND91-8001, Sandia National Laboratories.
- [68] Y. Ju, K. Maruta, Microscale combustion: technology development and fundamental research, *Prog. Energy Combust. Sci.* 37 (2011) 669–715.